CORA Cork Open Research Archive
Cartlann Taighde Oscailte Chorcaí

Title	Rotor configuration effects on coupled aero-hydro-mooring dynamics of spar-type floating vertical axis wind turbines
Authors	Dai, Jiarui;Huang, Haoda;Liu, Qingsong;Li, Chun;Iglesias, Gregorio;Bashir, Musa
Publication date	2026-05-29
Original Citation	Dai, J, Huang, H, Liu, Q, Li, C, Iglesias, G & Bashir, M 2026, 'Rotor configuration effects on coupled aero-hydro-mooring dynamics of spar-type floating vertical axis wind turbines', Energy, vol. 359, 141495, pp. 1-22. https://doi.org/10.1016/j.energy.2026.141495
Type of publication	Article (peer-reviewed)
Link to publisher's version	https://www.scopus.com/pages/publications/105040656484 - 10.1016/j.energy.2026.141495
Rights	© 2026, authors. Published by Elsevier Ltd. This is an open access article under the CC BY license (http://creativecommons.org/licenses/by/4.0/) - https://creativecommons.org/licenses/by/4.0/
Download date	2026-11-14 16:12:45
Item downloaded from	https://hdl.handle.net/10468/19532

UCC
University College Cork, Ireland
Coláiste na hOllscoile Corcaigh

Energy 359 (2026) 141495

Contents lists available at ScienceDirect

Energy

journal homepage: www.elsevier.com/locate/energy

Rotor configuration effects on coupled aero-hydro-mooring dynamics of spar-type floating vertical axis wind turbines

Jiarui Dai [a], Haoda Huang [a,b], Qingsong Liu [b,*], Chun Li [a], Gregorio Iglesias [b,c], Musa Bashir [d]

[a] School of Energy and Power Engineering, University of Shanghai for Science and Technology, Shanghai, 200093, China
[b] School of Engineering and Architecture, University College Cork, College Rd., Cork, T12 K8AF, Ireland
[c] School of Engineering, Computing and Mathematics, University of Plymouth, Drake Circus, Plymouth, PL4 8AA, United Kingdom
[d] School of Engineering, University of Liverpool, The Quadrangle, Brownlow Hill, L69 3GH, United Kingdom

ARTICLE INFO

Keywords:
Floating vertical axis wind turbine
Spar platform
Computational fluid dynamics
Dynamic fluid-body interaction
Darrieus rotor

ABSTRACT

The selection of the rotor configuration for floating vertical axis wind turbines (VAWTs) plays a major role in their energy capture efficiency and structural reliability. The objective of this work is to investigate the differences in performance between different rotor configurations and to clarify the dominant coupling mechanisms under floating conditions. A high-fidelity computational fluid dynamics (CFD) framework is established by combining dynamic fluid-body interaction (DFBI) and volume of fluid (VOF) models to capture the fully coupled aero-hydrodynamic response. A comparative analysis of full-scale H-type and Φ-type floating VAWTs with the same swept area is performed. The results show that the more compact support structure of the Φ-type rotor reduces flow losses, leading to a higher time-averaged power coefficient of 0.378, compared with 0.201 for the H-type rotor. Although the H-type rotor generates higher torque on the upwind side, its overall power output is weakened by downwind torque fluctuation, tip-vortex effects, and support-arm interference. The wake of the H-type rotor shows stronger flow disturbance and lateral diffusion, while the Φ-type rotor maintains a more coherent downstream wake due to its closed blade-end connections. Due to its larger upwind projected area, the thrust coefficient of the H-type rotor is approximately 9% higher than that of the Φ-type rotor, resulting in larger surge drift and a redistribution of mooring tensions. These findings provide guidance for the rotor–platform integration of floating VAWTs and highlight key design trade-offs that should be considered in future large-scale offshore deployments.

Nomenclature

Acronyms	
2-D	Two-dimensional
3-D	Three-dimensional
6-DOF	Six degrees of freedom
CFD	Computational Fluid Dynamics
CFL	Courant-Friedrichs-Lewy number
CM	Center of Mass
DFBI	Dynamic Fluid-Body Interaction
DES	Detached-eddy simulation
DMSM	Double multiple streamtube model
FOWT	Floating Offshore Wind Turbine
GCI	Grid Convergence Index
HAWT	Horizontal axis wind turbine
ML	Mooring Line
PSD	Power Spectral Density
SST	Shear Stress Transport
TSR	Tip speed ratio
URANS	Unsteady Reynolds-Averaged Navier–Stokes
VAWT	Vertical Axis Wind Turbine
VOF	Volume of Fluid

Symbols	
c	Blade chord length [m]
C_d	Drag coefficient [−]
C_l	Lift coefficient [−]
C_M	Torque coefficient [−]
C_P	Power coefficient [−]
C_T	Thrust coefficient [−]
f_b	Blade passing frequency [Hz]
f_w	Wave frequency [Hz]
M	Torque [N·m]
n	Rotational speed [rpm]
P	Power [kW]
R	Rotor radius [m]
T	Thrust [N]
V_∞	Free-stream wind velocity [m/s]
$y+$	Dimensionless Wall Distance [−]
α	Angle of attack [°]
β	Blade Pitch Angle [°]
λ	Tip speed ratio [−]
ρ	Air density [kg/m^3]
ω_r	Rotational angular velocity [rad/s]

(*continued on next column*)

(*continued*)

* Corresponding author.
E-mail address: QLiu@ucc.ie (Q. Liu).

https://doi.org/10.1016/j.energy.2026.141495
Received 21 March 2026; Received in revised form 19 May 2026; Accepted 26 May 2026
Available online 27 May 2026
0360-5442/© 2026 The Authors. Published by Elsevier Ltd. This is an open access article under the CC BY license (http://creativecommons.org/licenses/by/4.0/).

1. Introduction

1.1. Research background

Against the backdrop of the escalating global climate crisis, the transition from fossil fuels to low-carbon, renewable energy sources is widely regarded as a key pathway to mitigating climate change [1]. As an essential component of renewable energy, wind energy has gained increasing importance in the global energy transition due to its significant emission reduction potential and continuously improving cost competitiveness [2]. With high-quality nearshore sites becoming increasingly limited, offshore wind development is gradually moving towards deeper and more distant waters. However, the installation costs of traditional bottom-fixed wind turbines increase sharply with water depth, which has driven the development of floating offshore wind turbines (FOWTs) [3,4].

Based on the orientation of the rotational axis, wind turbines can be broadly classified into horizontal axis wind turbines (HAWTs) and vertical axis wind turbines (VAWTs). In current engineering practice, HAWTs remain dominant in offshore wind energy due to their high aerodynamic efficiency and mature industry supply chain [5]. However, the shift towards floating platforms and larger-capacity turbines has increased aero-structural coupling challenges. Platform motions continuously change the rotor inflow, while turbine upscaling increases blade and tower flexibility, making the system more sensitive to unsteady loads and fatigue accumulation [6]. In this context, VAWTs have regained increasing research interest [7,8]. Their insensitivity to wind direction, lower overall center of gravity, and reduced reliance on tall towers and ultra-long flexible blades make them attractive for floating offshore applications [9–11]. According to the operating principles, VAWTs can be further divided into lift-based Darrieus rotors and drag-based Savonius rotors [12,13]. Among them, lift-type Darrieus VAWT, characterized by relatively high aerodynamic efficiency and promising engineering application potential, has attracted widespread attention. Two representative Darrieus configurations are the straight-bladed H-type and the curved-bladed Φ-type (troposkien-type) [14,15]. From an aerodynamic perspective, the H-type rotor uses straight blades connected to the central shaft by horizontal support arms, leaving free blade tips that may induce tip vortices and support-arm interference. In contrast, the Φ-type rotor uses curved blades with closed blade-end connections and shorter root-concentrated supports, which changes the blade loading and wake development.

1.2. Research status

1.2.1. Numerical methods for floating VAWTs

The performance assessment of floating VAWTs involves complex interactions among aerodynamic loads, wave-induced hydrodynamic loads, platform motions and mooring restoring forces. Numerical methods are therefore essential for evaluating the dynamic behavior of floating VAWTs under different operating and environmental conditions, especially for full-scale systems where experimental testing remains costly and difficult [16].

Two-dimensional (2-D) models are commonly used for rapid aerodynamic prediction and preliminary design of VAWTs. Previous studies have applied 2-D CFD models to investigate pitching effects, pitch control strategies, airfoil selection, and turbine interaction characteristics [17–19]. These studies provide useful insights into aerodynamic load variation and power optimization. However, 2-D models neglect blade-tip vortices, support-induced three-dimensional flow structures, and platform-motion-induced inflow variations. Therefore, they are limited in resolving the complex flow physics and coupled dynamic responses of floating VAWTs.

In contrast, three-dimensional (3-D) CFD models can capture rotational effects, vortex separation, blade-tip vortices, and wake evolution more accurately. Lei et al. [20] investigated the influence of prescribed periodic pitching motion on the unsteady aerodynamic performance of an H-type floating VAWT, using the improved delayed DES (IDDES) method. Their results revealed that pitching motion can intensify aerodynamic load fluctuations by changing the relative inflow conditions. After that, Lei et al. [21] further investigated the effects of heave and pitch motions on the wake characteristics of an H-type VAWT and demonstrated that platform motions can alter wake displacement, velocity deficit, and vortex interaction. For the Φ-type configuration, Su et al. [22] studied the impact of platform heave on the aerodynamic performance and found that heave motion can increase the average power coefficient while also strengthening torque and thrust fluctuations. Although these 3-D studies provide more detailed descriptions of flow-field and wake structures, most of them used predefined sinusoidal or cosine platform motions within decoupled frameworks, which cannot fully represent the irregular responses of floating systems under realistic wind-wave loading, where platform motions are governed by the coupled action of aerodynamic loads, hydrodynamic loads, and mooring restoring forces.

Therefore, coupled simulations are needed to capture the force-motion feedback of floating VAWTs under realistic marine conditions. Guo et al. [23] developed a MATLAB-based in-house simulation code by integrating Double Multiple Streamtube Model (DMSM), potential flow theory, and the Morison equation to predict the coupled response of a 5 MW Φ-type VAWT. Their findings demonstrated that the use of a heave plate reduced heave motion and helped avoid the dominant wave and aerodynamic excitation frequencies. Lee et al. [24] developed a fully coupled dynamic analysis tool for floating counter-rotating VAWTs based on FAST, DMSM, HydroDyn, and MoorDyn, showing that the counter-rotating layout can reduce structural loads and platform motions through torque cancellation. Cheng et al. [25] employed the SIMO-RIFLEX-AC code to compare the extreme and fatigue responses of HAWTs and VAWTs mounted on a semi-submersible platform, highlighting the importance of blade number and mooring load assessment. These studies demonstrate the importance of coupled analysis for predicting floating wind turbine responses. Nevertheless, many existing models are still based on medium-to-low fidelity aerodynamic or hydrodynamic methods, which limit their ability to resolve detailed wake structures, support-induced flow interference, and complex aero-hydrodynamic interactions.

In recent years, CFD-based coupled frameworks combining DFBI and VOF have been increasingly adopted for floating VAWT analysis under combined wind-wave conditions. Luo et al. [26] investigated the load characteristics and extreme responses of a straight-bladed floating VAWT. Yang et al. [27] examined the coupled dynamic response and energy conversion characteristics of a 10 MW floating VAWT with different configurations. Xie et al. [28] analyzed a floating VAWT with enhanced Spar platforms designed to improve hydrodynamic stability, while Liu et al. [29] studied the aero-hydrodynamic interactions of floating VAWTs in staggered configurations. These studies have advanced the application of high-fidelity CFD simulations to floating VAWTs. However, most existing works still focus on a single rotor type, specific platform improvements, or array-layout effects. A direct full-scale comparison between H-type and Φ-type rotors under identical Spar platform, swept area, blade number, mooring layout, and wind-wave conditions remain limited. Therefore, how rotor configuration affects aerodynamic efficiency, wake evolution, platform motions, and mooring tensions within an integrated floating system is still not fully understood.

1.2.2. Floating platform application

Floating platforms are generally classified into four main categories: barge, tension-leg, semi-submersible, and Spar platforms [30,31]. The platform type strongly affects the motion characteristics, restoring behavior, and load transfer mechanism of floating wind turbine systems. Among these concepts, the Spar platform has been widely studied and applied in offshore wind research due to its deep draft, low center of

gravity, and favorable hydrodynamic stability [32,33]. For example, the 1 MW floating prototype planned by Sea Twirl for commercial deployment in the Bokn area of Norway adopted a Spar-type floating foundation [34]. Table 1 summarizes representative studies on Spar-type floating wind turbine systems.

As shown in Table 1, although Spar-type platforms have been widely investigated in floating wind turbine research, most existing studies have focused on HAWTs. Their platform dimensions, stability characteristics, and mooring layouts are therefore mainly developed according to the load distribution and structural layout of HAWTs. In contrast, the coupled behaviour of Spar-type floating VAWTs remains less understood. This issue is particularly important because VAWTs differ from HAWTs in aerodynamic load distribution, center-of-gravity arrangement, rotor-support layout, and wake development. Moreover, for Darrieus-type VAWTs, different rotor configurations may induce different thrust loads, wake structures, platform motions, and mooring tensions. Therefore, it is necessary to assess H-type and Φ-type rotors on the same Spar-type floating platform, so that the influence of rotor configuration can be separated from platform and mooring-layout effects.

1.3. Research content

In light of the above research gaps, this study conducts a full-scale numerical comparison of H-type and Φ-type VAWTs mounted on the same Spar-type floating platform under combined wind-wave loading. The main novelty lies in isolating the effect of rotor configuration within a unified floating system and linking rotor geometry to aerodynamic performance, wake evolution, platform 6-DOF motion, and mooring line tensions. Compared with previous floating VAWT studies that mainly focused on single configurations, prescribed platform motions, or medium-to-low fidelity models, this study employs a CFD-based high-fidelity coupled framework to provide a clearer system-level understanding of the aero-hydro-mooring mechanisms governing H-type and Φ-type Spar-type floating VAWTs. The main contributions of this study are summarized as follows:

(1). A unified full-scale comparative framework is established for H-type and Φ-type floating VAWTs. The two configurations are designed with identical swept area and mounted on the same Spar-type floating platform. This setup ensures that the observed differences in dynamic response and overall performance are mainly caused by rotor configuration rather than platform or environmental differences.

(2). A CFD-based aero-hydro-mooring analysis framework is developed in STAR-CCM+. The VOF method is used to resolve the air-water interface and incident wave field, while the DFBI solver updates the rotor rotation and platform 6-DOF motion. The catenary mooring model provides restoring forces according to the instantaneous fairlead positions.

(3). The configuration-dependent response mechanisms of H-type and Φ-type floating VAWTs are systematically examined in terms of power output, flow-field and wake evolution, 6-DOF responses, and mooring line tension. The analysis further explains how blade geometry, support-arm layout, tip-vortex behavior, and aero-hydrodynamic coupling jointly affect energy capture and global dynamic stability.

Table 1
Representative studies on HAWTs and VAWTs mounted on Spar-type floating platforms.

References	Institution	Year	Project	Type
Liu et al. [35]	NBU, China	2025	NSFC	15 MW HAWT
Ojo et al. [36]	Strath, UK	2025	EPSRC	5 MW HAWT
Somoano et al. [37]	UC, Spain	2024	COREWIND	15 MW HAWT
Ran et al. [38]	NTNU, Norway	2023	WEAMEC	10 MW HAWT
Inceptive Mind [34]	Sea Twirl	2022	S2x	1 MW VAWT
Beshbichi et al. [39]	UiS, Norway	2022	EAP	10 MW HAWT
Xu et al. [40]	Strath, UK	2021	EFS	5 MW HAWT
Yue et al. [41]	USST, China	2020	NSFC	5 MW HAWT
Borg M et al. [42]	Cranfield, UK	2015	NOVA	5 MW VAWT

The remainder of this paper is organized as follows: Section 2 presents the geometric modeling of the two VAWT configurations and the parameter definitions used in this study. Section 3 introduces research methods and models, including the DFBI method and the VOF wave model. Section 4 describes the computational domain and mesh generation for the numerical simulations, along with turbulence model validation and hydrodynamic performance verification. Section 5 discusses the simulation results of the two VAWT configurations, focusing on aerodynamic analysis, hydrodynamic analysis, and power spectral density analysis. Section 6 presents the conclusions drawn from this study.

2. Geometric modeling

2.1. Environmental loads

Fig. 1 illustrates the coupled dynamic behavior of the H-type and Φ-type VAWTs under combined wind-wave loading. Under the combined action of wind and wave loads, the floating VAWT undergoes 6-DOF motion, including surge, sway, heave roll, pitch, and yaw. The platform's dynamic equilibrium is maintained through restoring forces and moments provided by the mooring system. During operation, interactions arise among rotor aerodynamic loads, platform motion responses, and variations in mooring tension, resulting in pronounced unsteady behaviors and strong coupling effects. At the same time, free surface dynamics at the air-water interface and flow field disturbances introduce high-order hydrodynamic loads, further intensifying the system's nonlinear dynamic response.

2.2. Geometric model

Fig. 2 presents the full-scale geometric models of the floating H-VAWT and Φ-VAWT in this study, including the two rotor configurations, and the OC3 Spar platform. The geometric model of the H-type VAWT is based on the work conducted by Liu et al. [43], with the detailed geometric parameters provided in Table 2.

In Fig. 2, the horizontal support rods are generated by sweeping NACA airfoils with varying thickness and chord lengths, with the specific shape, spatial location, and chord length of each airfoil shown in Fig. 3. The tower is formed by sweeping circular cross-sections of S7, S8, and S9, with diameters of 5.5 m, 5 m, and 3 m, respectively.

In this study, the Φ-type VAWT uses the same DU-06-W-200 airfoil as the H-type VAWT, with identical blade shape parameters. The primary difference lies in the blade sweep direction, which follows the blue parabolic curve shown in Fig. 2. The blade height, H_2, is 90 m, and the rotor radius, R_2, is 45 m. The blade span, calculated via line integration along the curved blade axis, is 132.77 m. Notably, the swept areas of the H-type and Φ-type VAWTs used in this study are identical, as shown in Fig. 2, corresponding to the area enclosed by the blue parabolic curve envelope for the Φ-type rotor and the orange rectangular envelope for the Φ-type rotor, respectively.

The principal geometric dimensions of the OC3 Spar platform adopted in this study are presented in Fig. 2, with detailed physical parameters listed in Table 3. Additionally, to ensure platform stability, three mooring lines are used to anchor the platform to the seabed, arranged at 120° azimuthal angles. The detailed mooring parameters are given in Table 4.

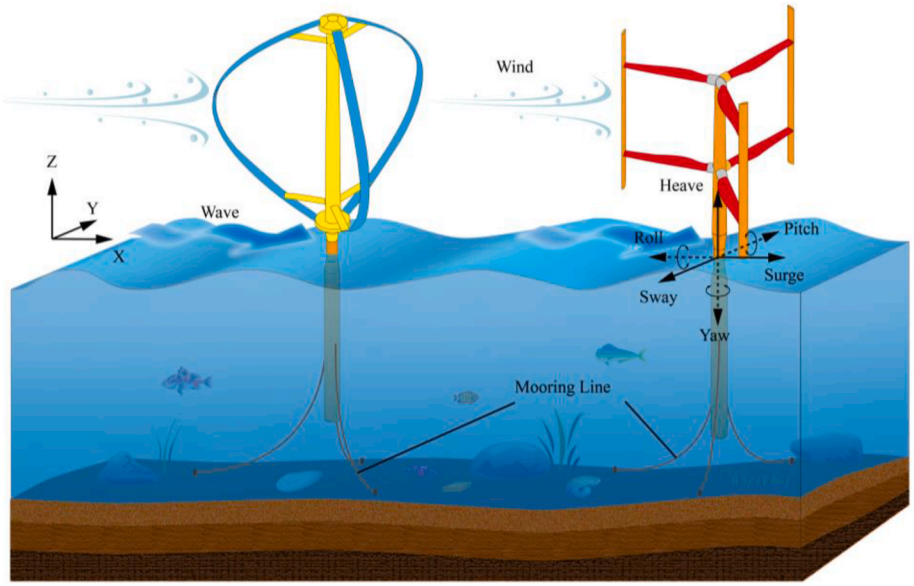


Fig. 1. Schematic of loads and 6-DOF motions of the H-type and Φ-type floating VAWT.

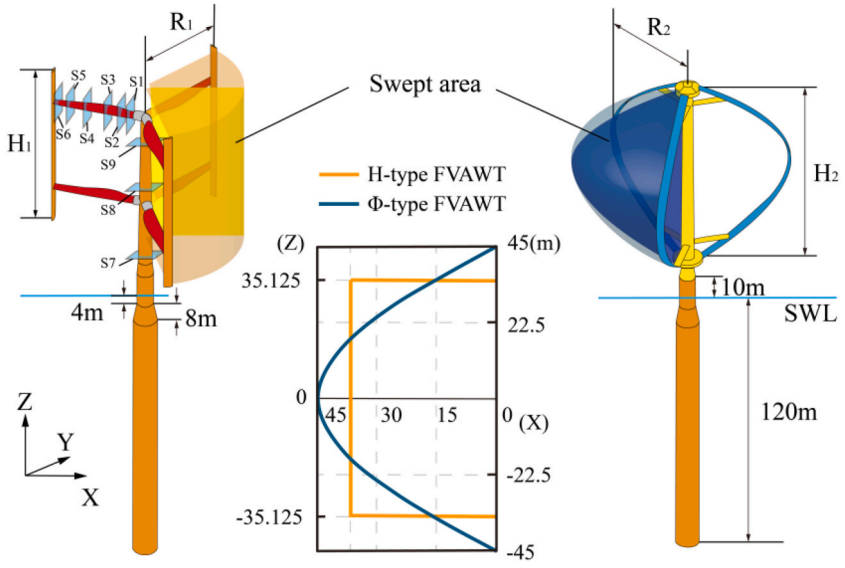


Fig. 2. Geometric models of H-type and Φ-type floating VAWT.

Table 2
Geometric parameters of the H-type VAWT.

Parameter	Value
Blade airfoil	DU-06-W-200
Number of blades	3
Number of support rods per blade	2
Blade height H_1	70.25 m
Rotor radius R_1	36.76 m
Blade chord length c	3.512 m
Blade pitch angle β	2°
Optimal tip speed ratio λ	3.28
Rated rotational speed ω	6.81 rpm

2.3. Parameter definitions

The tip speed ratio (TSR) is the ratio of the blade tip velocity to the wind speed. It reflects the motion state of the blade during wind turbine operation and has a significant impact on the efficiency of the turbine. It is expressed as:

$$\lambda = \frac{V_{tip}}{V_\infty} = \frac{\omega_r \cdot R}{V_\infty} = \frac{2\pi n \cdot R}{60 V_\infty} \tag{1}$$

In the equation, V_{tip} is the tip velocity of the blade, V_∞ is the freestream wind velocity at the blade height, ω_r is the rotational angular velocity of the rotor, R is the rotor radius, and n is the rotational speed of the wind turbine.

Aerodynamic thrust (F_T) refers to the force generated when the wind turbine blades interact with the incoming air, and it is an important parameter for assessing the impact of the wind turbine on the wind flow. Aerodynamic power (P_b) describes the capability of the wind turbine to capture and convert wind energy into mechanical energy. These are expressed as:

$$F_T = F_L \cdot \cos\alpha + F_D \cdot \sin\alpha \tag{2}$$

$$P_b = \omega_r \cdot M_b \tag{3}$$

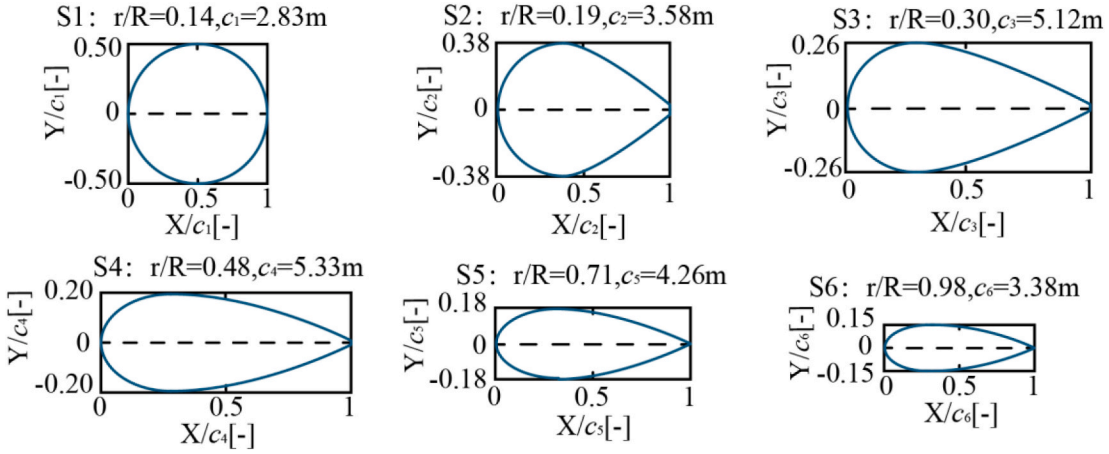


Fig. 3. Airfoil profiles and positions of the horizontal support rods.

Table 3
Main parameters of OC3 Spar platform.

Properties	Value
Spar platform mass	7.46×10^6 kg
Platform CM position	89.92 m
Roll inertia	4.23×10^9 kg•m^2
Pitch inertia	4.23×10^9 kg•m^2
Yaw inertia	1.64×10^8 kg•m^2

Table 4
Main parameters of the mooring system.

Properties	Value
Angle of arrangement	120°
Fairlead depth	70 m
Fairlead radius	5.2 m
Anchor depth	320 m
Anchor radius	853.87 m
Unstretched length	902.2 m
Equivalent density	77.71 kg/m
Equivalent extensional stiffness	3.84×10^8 N

In the equation, F_L and F_D represent the lift and drag forces generated by the blade, respectively; α is the blade's angle of attack, defined as:

$$\alpha = \arctan\left(\frac{\sin\varphi}{\lambda + \cos\varphi}\right) \tag{4}$$

In the equation, φ is the azimuth angle, representing the rotational angle of the wind turbine blades.

To facilitate a concise and intuitive non-dimensional expression of the wind turbine performance, this study uses the thrust coefficient, power coefficient, and torque coefficient as performance metrics. The thrust coefficient (C_T) is the ratio of the thrust generated by the wind turbine blades to the aerodynamic theoretical value, and it is used to describe the efficiency of thrust generation by the wind turbine. It is expressed as:

$$C_T = \frac{2F_T}{\rho V_\infty^2 A} \tag{5}$$

In the equation, ρ is the freestream air density, and A is the swept area.

The power coefficient (C_P) is an important parameter for evaluating the energy conversion efficiency of the wind turbine. It represents the ratio of the energy captured by the wind turbine from the wind to the total wind energy available. It is expressed as:

$$C_P = \frac{2P_b}{\rho V_\infty^3 A} = \frac{2\omega_r M_b}{\rho V_\infty^3 A} \tag{6}$$

The torque coefficient (C_M) is a parameter that measures the relationship between the torque generated by the wind turbine blades and the wind energy. It is related to the power coefficient and influences the rotational speed control of the wind turbine.

$$C_M = \frac{2M_b}{\rho V_\infty^2 AR} = \frac{C_P}{\lambda} \tag{7}$$

3. Numerical modeling

3.1. DFBI framework

The DFBI method is a numerical approach that couples the fluid governing equations and rigid body motion equations in the time domain [44]. The principle of the method is to simultaneously solve the fluid field and update the rigid body's 6-DOF motion in real-time, considering the impact of rigid body motion on the fluid. This enables a two-way real-time coupling calculation between the fluid field and the rigid body.

The governing equations for the fluid, namely the Navier-Stokes equations, are expressed as follows:

$$\frac{\partial \mathbf{u}}{\partial t} + (\mathbf{u}\cdot\nabla)\mathbf{u} = -\frac{1}{\rho}\nabla p + \nu\nabla^2\mathbf{u} + \mathbf{f} \tag{8}$$

In the equation, $\mathbf{u}$ is the fluid velocity vector, $\mathbf{u} = [u, v, w]^T$; ρ, p, and ν represent the fluid density, pressure, and kinematic viscosity, respectively; $\mathbf{f}$ denotes the body forces acting on the fluid.

The governing equations for the 6-DOF translational motion of the body are as follows:

$$m\frac{d\mathbf{v}}{dt} = \mathbf{f}_{tot} \tag{9}$$

In the equation, m is the mass of the rigid body, $\mathbf{f}_{tot}$ is the total external force acting on the rigid body, and $\mathbf{v}$ is the velocity of the center of mass of the rigid body.

The governing equations for the rotational motion in the center-of-mass coordinate system are as follows:

$$\mathbf{m}\frac{d\boldsymbol{\omega}}{dt} + \boldsymbol{\omega}\times\mathbf{m}\boldsymbol{\omega} = \mathbf{M} \tag{10}$$

$$\mathbf{m} = \begin{pmatrix} m_{xx} & m_{xy} & m_{xz} \\ m_{yx} & m_{yy} & m_{yz} \\ m_{zx} & m_{zy} & m_{zz} \end{pmatrix} \tag{11}$$

In the equation, **ω** is the angular velocity vector, **M** is the total external moment acting on the rigid body, and **m** is the inertia tensor. Due to the symmetry of the tensor, it can be defined using the principal moments of inertia $(m_{xx} \quad m_{yy} \quad m_{zz})$ and the inertia product $(m_{xy} \quad m_{xz} \quad m_{yz})$.

The computational framework of the DFBI method is shown in Fig. 4. By introducing the Reynolds-averaged Navier-Stokes equations combined with the SST *k-ω* turbulence model, it effectively captures the aerodynamic characteristics of the blade boundary layer and flow separation phenomena. The flow field is solved using the incompressible unsteady RANS equations, and the SST *k-ω* turbulence model is adopted for turbulence closure. The SST *k-ω* model combines the near-wall advantages of the *k-ω* model with the free-stream robustness of the *k-ε* model. It is therefore suitable for VAWT simulations involving adverse pressure gradients, blade flow separation, and dynamic stall. The governing transport equations of the SST *k-ω* turbulence model are expressed as:

$$\frac{\partial(\rho k)}{\partial t}+\frac{\partial(\rho u_i k)}{\partial x_i}=\frac{\partial}{\partial x_j}\left(\Gamma_k\frac{\partial k}{\partial x_j}\right)+G_k-Y_k+S_k \tag{12}$$

$$\frac{\partial(\rho \omega)}{\partial t}+\frac{\partial(\rho u_i \omega)}{\partial x_i}=\frac{\partial}{\partial x_j}\left(\Gamma_\omega\frac{\partial \omega}{\partial x_j}\right)+G_\omega-Y_\omega+D_\omega+S_\omega \tag{13}$$

In the equation, k is the turbulent kinetic energy, ω is the specific dissipation rate, G_k and G_ω are the turbulent kinetic energy generated by velocity gradients, Γ_k and Γ_ω are the effective diffusion terms induced by turbulent motion, Y_k and Y_ω are the turbulent dissipation terms, D_ω is the cross-dissipation term, and S_k and S_ω are the user-defined source terms.

The mooring system is modeled using the catenary model, while the free surface is modeled using the VOF method, accounting for the gas-water interaction. The aerodynamic, hydrodynamic, and mooring forces acting on the VAWT are then passed to the 6-DOF solver, which updates the state at each time step using an overset mesh, providing dynamic responses for all components. In this study, considering that the global motion of the floating system is much larger than the elastic deformation of the blades, the VAWT is simplified to a rigid body model for the calculations, avoiding the complexity of structural dynamics. This simplification allows the DFBI method to efficiently simulate the dynamic behavior of the wind turbine, providing suitable results for design optimization and performance evaluation.

In the DFBI method, the mooring system is described using the quasi-static catenary equation. In the Cartesian coordinate system, the shape of the mooring line is given by the following parametric equations:

$$\begin{cases} x(\theta)=\psi_1\theta+\psi_2\sinh(\theta)+t_1 \\ y(\theta)=\psi_1\cosh(\theta)+\dfrac{\psi_2}{2}\sinh^2(\theta)+t_2 \\ \theta_1\le\theta\le\theta_2 \end{cases} \tag{14}$$

In the equation, t_1 and t_2 are integration constants, which are related to the total mass of the mooring line and the positions of the two endpoints; θ is the variable in the parametric equation, with θ_1 and θ_2 describing the positions of the two mooring endpoints, representing the range of θ. The constants ψ_1, ψ_2, and ψ_3 are defined as follows:

$$\begin{cases} \psi_1=\dfrac{\psi_3}{\lambda_0 g} \\ \psi_2=\dfrac{\psi_1\psi_3}{EIL_0} \\ \psi_3=\dfrac{\lambda_0 L_0 g}{\sinh(\theta_2)-\sinh(\theta_1)} \end{cases} \tag{15}$$

In the equation, λ_0 is the linear density of the mooring, g is the gravitational acceleration, EI is the mooring stiffness, L_0 is the unstretched length of the mooring, and F_1 and F_2 are the forces acting on the two ends of the mooring, with their directions aligned with the tangent direction of the connection points. These are specifically expressed as:

$$[F_1 \quad F_2]=\begin{bmatrix} F_{1,x} & F_{2,x} \\ F_{1,y} & F_{2,y} \end{bmatrix}=\psi_3\begin{bmatrix} 1 & -1 \\ \sinh(\theta_1) & -\sinh(\theta_2) \end{bmatrix} \tag{16}$$

3.2. VOF wave model

In STAR-CCM+, the Volume of Fluid (VOF) wave model is an effective method used to simulate the interface variation in multiphase fluids, and is particularly suitable for simulating the dynamic evolution of free surfaces or air-liquid interfaces. The model describes the distribution of different phases by tracking and calculating the volume fraction function of each phase, and captures the changes in the phase interface within the numerical grid. The volume fraction ξ_i for each computational cell is defined as:

$$\xi_i=\frac{V_i}{V} \tag{17}$$

In the equation, V_i is the volume occupied by phase i within a cell of volume V. The volume fractions of the N phases must satisfy the following constraint:

$$\sum_{i=1}^{N}\xi_i=1 \tag{18}$$

In this study, there are two phases: water and air, with water being the primary phase. The volume fraction can be directly solved using the following transport equation:

$$\frac{\partial\xi_1}{\partial t}+\nabla\cdot[(\mathbf{u}-\mathbf{u}_m)\xi_1]+\nabla\cdot[\mathbf{u}_c(1-\xi_1)\xi_1]=0 \tag{19}$$

In the equation, ξ_1 is the volume fraction of water, $\mathbf{u}_m$ is the mesh

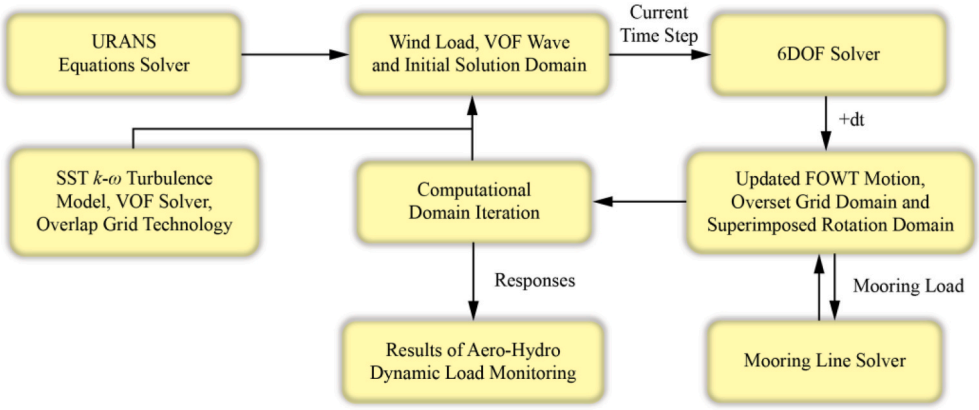


Fig. 4. DFBI framework of the floating VAWT.

velocity vector, and $\mathbf{u}_c$ is the compressive term of the velocity vector. The volume fraction of air, ξ_2, can be obtained through the constraint $\xi_1 + \xi_2 = 1$ as shown in equation (18).

Stokes waves theory is used to describe surface waves and is suitable for modeling nonlinear wave behavior. Compared to the first-order Stokes wave model, the fifth-order Stokes wave considers higher-order nonlinear effects of the waves, providing a more accurate description. To assess the applicability of the Stokes model, the dimensionless Ursell number U_r [45] is introduced:

$$U_r = \frac{\varepsilon}{\mu^2} = \frac{(H/h)}{(h/\lambda)^2} = \frac{H\lambda^2}{h^3} \tag{20}$$

In the equation, ε and μ are the nonlinear and dispersion parameters, respectively; H is the wave height, λ is the wavelength, and h is the average water depth. When $U_r < 30$, the fifth-order Stokes wave model is applicable. The advantage of the VOF model lies in its ability to handle complex flow phenomena, including wave propagation, droplet formation and coalescence, and free surface fluctuations, making it suitable for flow problems with significant interface deformation.

Based on the above descriptions, a coupled aero-hydro-mooring solution framework is established in STAR-CCM + by combining the VOF multiphase model, the DFBI motion solver, and the catenary mooring model. The VOF model captures the air-water interface and incident wave field, while the CFD solver calculates the instantaneous aerodynamic and hydrodynamic loads acting on the rotor, tower, and floating platform. At each physical time step, these loads, together with gravity, buoyancy, and mooring restoring forces, are passed to the DFBI solver to update the 6-DOF motion of the floating system. The updated platform motion changes the positions of the rotor, floater, and fairlead points. The computational mesh and overset regions are then updated, and the mooring restoring forces are recalculated from the catenary model according to the new fairlead positions. Through this time-marching force-motion feedback, the aerodynamic loads, wave-induced hydrodynamic loads, platform motions, and mooring responses are solved in a coupled manner under combined wind-wave loading.

4. Reliability validation of the numerical model

4.1. Numerical setup and verification

The boundary conditions for the computational domain of the H-type VAWT and Φ-type VAWT are shown in Fig. 5. The size of the computational domain is 1200 m (X) × 500 m (Y) × 600 m (Z), with a water depth of 320 m. The upstream boundary is a velocity inlet, the downstream boundary is a pressure outlet, and the bottom surface is set as a wall. The side walls and the upper surface are set as symmetry planes. The air density is set to 1.225 kg/m^3, and the seawater density is 1025 kg/m^3. The wind and wave boundary conditions used in the simulations are summarized in Table 5. The anchor points of the three mooring lines are located on the seabed outside the computational domain. A wave damping zone is set downstream to eliminate the effect of reflected waves, starting 500 m upstream of the pressure outlet. Additionally, overset domains are used to simulate the rotation of the vertical axis wind turbine and the 6-DOF motion of the platform. Three overset regions are included: the overset region 1 between the rotor rotation domain and the computational domain, the overset region 2 between the platform motion domain and the computational domain, and the overset region 3 between the rotation domain and the platform motion domain.

Fig. 6 shows the mesh distribution for the two floating VAWT configurations. The computational domain is discretized using a cutting volume mesh generator, with local refinement implemented around the rotor, structural surfaces, and the free surface area to capture critical flow features while balancing the overall computational cost. This mesh strategy helps improve solution accuracy and numerical stability, thus enabling a more reliable simulation of complex flows and wave-floating body interaction processes. The background domain grid size used in this study is 10 m, while the platform and the rotor domains of the H-type VAWT and Φ-type VAWT use a grid size of 1.25 m. To accurately capture the flow characteristics of the boundary layer near the blades, prismatic layer meshes with a first layer thickness of 5 × 10^{-3} m and 8 layers are generated within a 0.28 m near-wall region around the blades. Additionally, to precisely depict the development of the wind turbine wake and the wave propagation process, local refinement is applied to

Table 5
Wind and wave boundary conditions.

Parameter	Value
Wind speed	8 m/s
Wave height	7.58 m
Wave period	12.1 s
Water depth	320 m
Wave frequency	0.08268 Hz
Rotor rotational speed	6.81 rpm

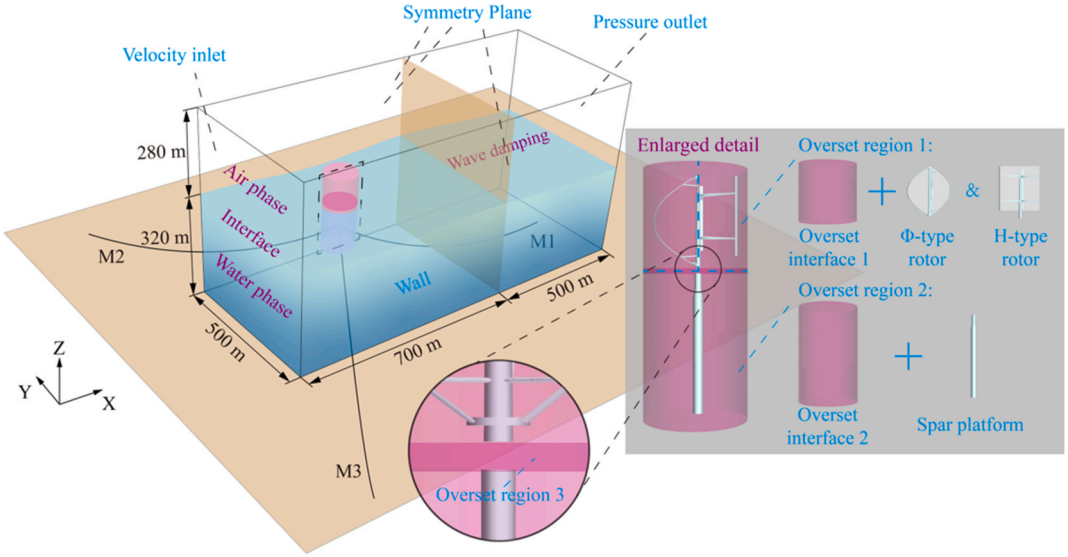


Fig. 5. Boundary conditions of the computational domain.

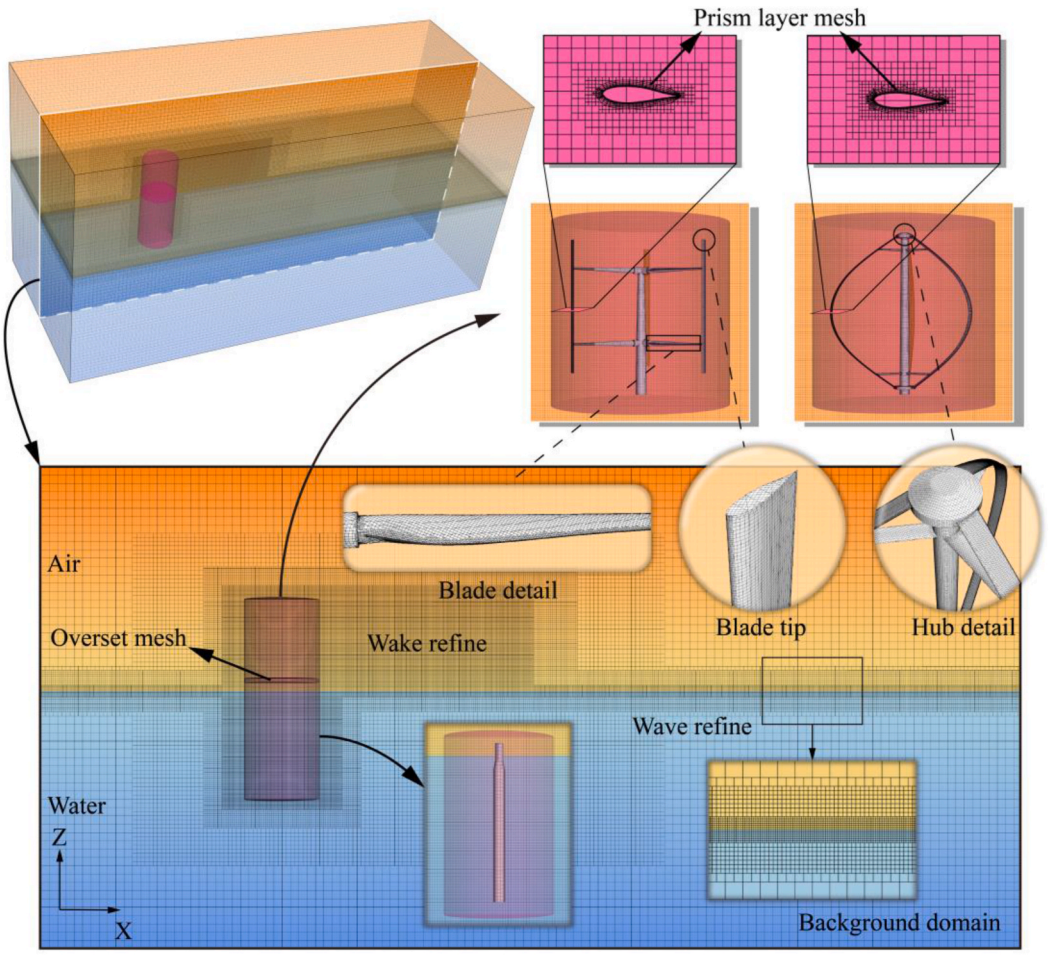


Fig. 6. Mesh distribution of the H-type and Φ-type floating VAWT.

the wake region downstream of the rotor and the air-water interface. The refined wake region extends 300 m downstream of the rotor to ensure sufficient resolution for wake evolution and development. The total number of grid nodes for the H-type VAWT is 14,056,545, with 10,904,940 nodes for the background domain, 575,516 nodes for the platform motion domain, and 2,576,089 nodes for the rotor rotation domain. For the Φ-type VAWT, a total of 15,269,643 grid nodes is obtained, with 10,904,940 nodes for the background domain, 686,389 nodes for the platform motion domain, and 3,678,314 nodes for the rotor rotation domain.

Given the full-scale nature of the simulated floating VAWTs, a fully wall-resolved mesh with $y+ \approx 1$ would require an extremely large cell count. Therefore, the near-wall mesh was mainly designed for the wall-function regime. The all-$y+$ wall treatment in STAR-CCM+ was adopted to accommodate local variations in $y+$ and to ensure a consistent near-wall treatment across the rotor surfaces. The wall $y+$ distributions on the blade surfaces of the two rotor configurations are shown in Fig. 7. As shown, most blade-surface regions fall within $50 \leq y+ \leq 150$, which is consistent with the commonly recommended range for wall-function-based SST k-ω simulations.

To verify grid independence, three mesh schemes with different resolutions were established for the two VAWT configurations, and the detailed mesh parameters are listed in Table 6. The rotor region cells include the mesh elements around the blades and support arms, while the Spar platform region cells represent the mesh elements around the Spar platform. The downstream wake refinement region extends 300 m downstream of the rotor, and its base size for each mesh level is listed in Table 6. The near-wall mesh settings, including the number of prism layers, first-layer height, total prism-layer thickness, and $y+$

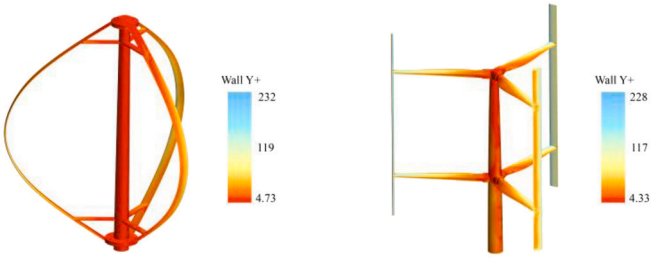


Fig. 7. $y+$ distributions on the blade surfaces for two rotor configurations.

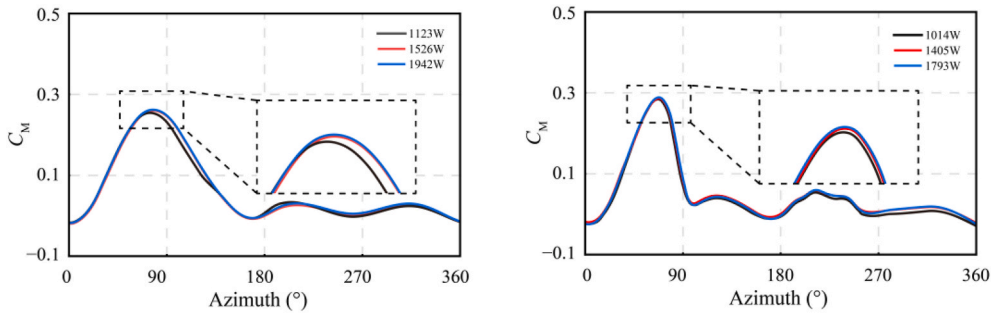
distributions, are described above. Table 6 also summarizes the main mesh-quality indicators, including average orthogonal quality, average skewness angle, and GCI.

The comparison of the torque coefficients C_M with azimuthal angle for the two VAWTs is shown in Fig. 8. It can be observed that the C_M curves nearly overlap even in the most sensitive zoomed regions. To further quantify the convergence, the grid convergence index GCI for the medium grid is calculated as 3.81% for the H-type and 6.42% for the Φ-type VAWT, both within acceptable ranges for engineering CFD simulations. Considering the balance between computational efficiency and cost, this study adopts the medium-resolution grid scheme for subsequent simulations.

To evaluate the influence of time-step size on the numerical results, four time steps, $\Delta t = 0.04$, 0.03, 0.02, and 0.01s, were tested using the

Table 6
Mesh parameters and quality metrics for the grid-independence study.

Parameters	Φ-VAWT			H-VAWT		
	Coarse	Medium	Fine	Coarse	Medium	Fine
Background base size (m)	11	10	9	11	10	9
Background region cells	7208070	10904940	14006320	7208070	10904940	14006320
Rotor base size (m)	1.375	1.25	1.125	1.375	1.25	1.125
Rotor region cells	3410432	3678314	4465437	2413889	2576089	3131915
Spar platform base size (m)	1.375	1.25	1.125	1.375	1.25	1.125
Spar platform region cells	618937	686389	952339	518987	575516	794798
Total cells	11237439	15269643	19424096	10140946	14056545	17933033
Downstream wake refinement base size (m)	1.375	1.25	1.125	1.375	1.25	1.125
Orthogonal quality (avg.)	0.909	0.910	0.912	0.924	0.928	0.932
Skewness angle (avg.)	9.721°	9.145°	8.853°	9.447°	8.832°	7.946°
GCI (%)	-	6.42	0.66	-	3.81	0.78



(a) C_M of Φ-type VAWT (b) C_M of H-type VAWT

Fig. 8. Mesh independence verification results of two VAWTs.

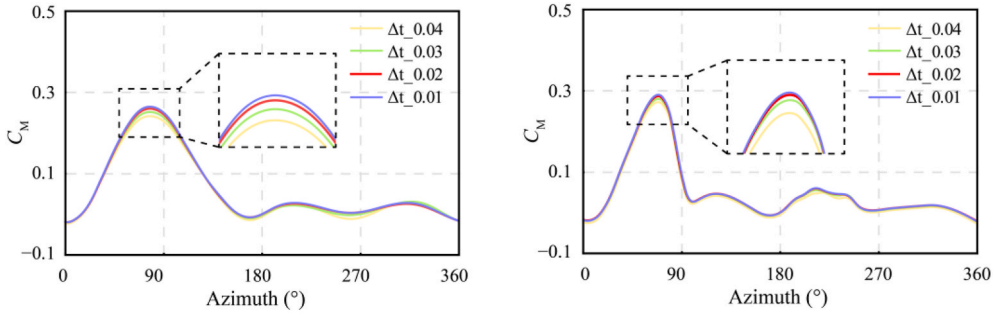
rotor torque coefficient as the monitored variable. As shown in Fig. 9, the torque coefficient curves show similar trends for all cases and gradually converge as the time step decreases. When the time step is reduced to 0.02 s or smaller, the difference in the torque coefficient becomes limited, and further refinement produces only minor changes. Considering both numerical accuracy and computational cost, Δt = 0.02 s is adopted as the final time step for all subsequent simulations in this study.

A CFL (Courant-Friedrichs-Lewy) analysis is performed to evaluate the temporal stability of the unsteady simulation. The CFL number is defined as:

$$\mathrm{CFL} = \frac{U \cdot \Delta t}{\Delta x} \tag{21}$$

where U is the characteristic flow velocity, Δt denotes the time step, and Δx is the local grid size. In the rotor region, the base grid size of 1.25 m, and the blade surface refinement ratio is 12.5%, giving a minimum local grid size of 0.15625 m. Using the inlet wind speed of 8 m/s and Δt = 0.02 s, the estimated CFL number in the refined blade region is approximately 1.024. Since the implicit unsteady solver is used in this study, this CFL level is acceptable for the present transient simulation.

The main solver settings are summarized as follows. The simulations are performed in STAR-CCM + using the segregated flow solver with an implicit unsteady scheme. The time step is set to 0.02 s, and second-order temporal discretization is adopted. The SST $k-\omega$ turbulence model is used for turbulence closure, while the VOF model captures the air-water interface and incident wave field. The DFBI model is coupled with the overset mesh method to resolve the platform 6-DOF motion and the prescribed rotor rotation. For spatial discretization, the convection terms of the momentum and turbulence equations are discretized using second-order upwind schemes to reduce numerical diffusion. The under-relaxation factor for the $k-\omega$ turbulence equations is set to 0.8, and that for turbulent viscosity is set to 1.0. The initial turbulence intensity and turbulence viscosity ratio are set to 0.01 and 10.0, respectively, while



(a) C_M of Φ-type VAWT (b) C_M of H-type VAWT

Fig. 9. Time-step independence verification results.

other solver parameters follow the default settings in STAR-CCM+.

4.2. Turbulence model validation

The SST k-ω turbulence model is adopted in the present simulation. This model has been widely used in wind turbine aerodynamic simulations because it combines the near-wall treatment of the k-ω model with the free-stream robustness of the k-ε model. It also has good capability in predicting adverse pressure gradients and separated flows, which are important for VAWT simulations involving dynamic stall and wake development. The reliability of the adopted turbulence model is assessed by comparison with the wind tunnel experiments reported by Battisti et al. [46] at Politecnico di Milano. The experimental setup is shown in Fig. 10 (a). In their low-turbulence wind tunnel, scaled H-type and Φ-type VAWTs were tested, providing benchmark data for three-dimensional numerical validation. The measured quantities include rotor power, longitudinal and lateral thrust, and wake velocity distributions.

Fig. 10 (b) shows the geometric model used for numerical computation, with geometric parameters consistent with the experimental model. Fig. 10 (c) presents the mesh discretization results of the computational domain in the numerical simulation. A total of 21 wake monitoring points were arranged at distances of 1.5R and 3R from the rotor's rotational center to validate the wake velocity. The mesh node count, obtained through the cutting-body mesh method, is 9,610,801. The SST k-ω turbulence model was used for turbulence closure and to model the boundary-layer flow near the blades. The time step of the simulation was 2.08×10^{-4} s, with the rotor rotating 0.5° per time step, and the total simulation time was 3 s. The data from the final stable rotational period was compared with the experimental results, as shown in Fig. 11. It can be observed that the power coefficients of both VAWTs are in good agreement with the experimental values within the selected operating conditions, with significant deviations only when TSR >3.8 for the Φ-type and TSR >3.2 for the H-type.

Fig. 12 compares the power coefficient and wake velocity distribution obtained from the present SST k-ω simulation with the experimental data at different TSRs. The results show good agreement with the measurements, indicating that the present CFD setup can reasonably predict the main aerodynamic performance and mean wake characteristics of the VAWT. It should be noted that a separate turbulence-model

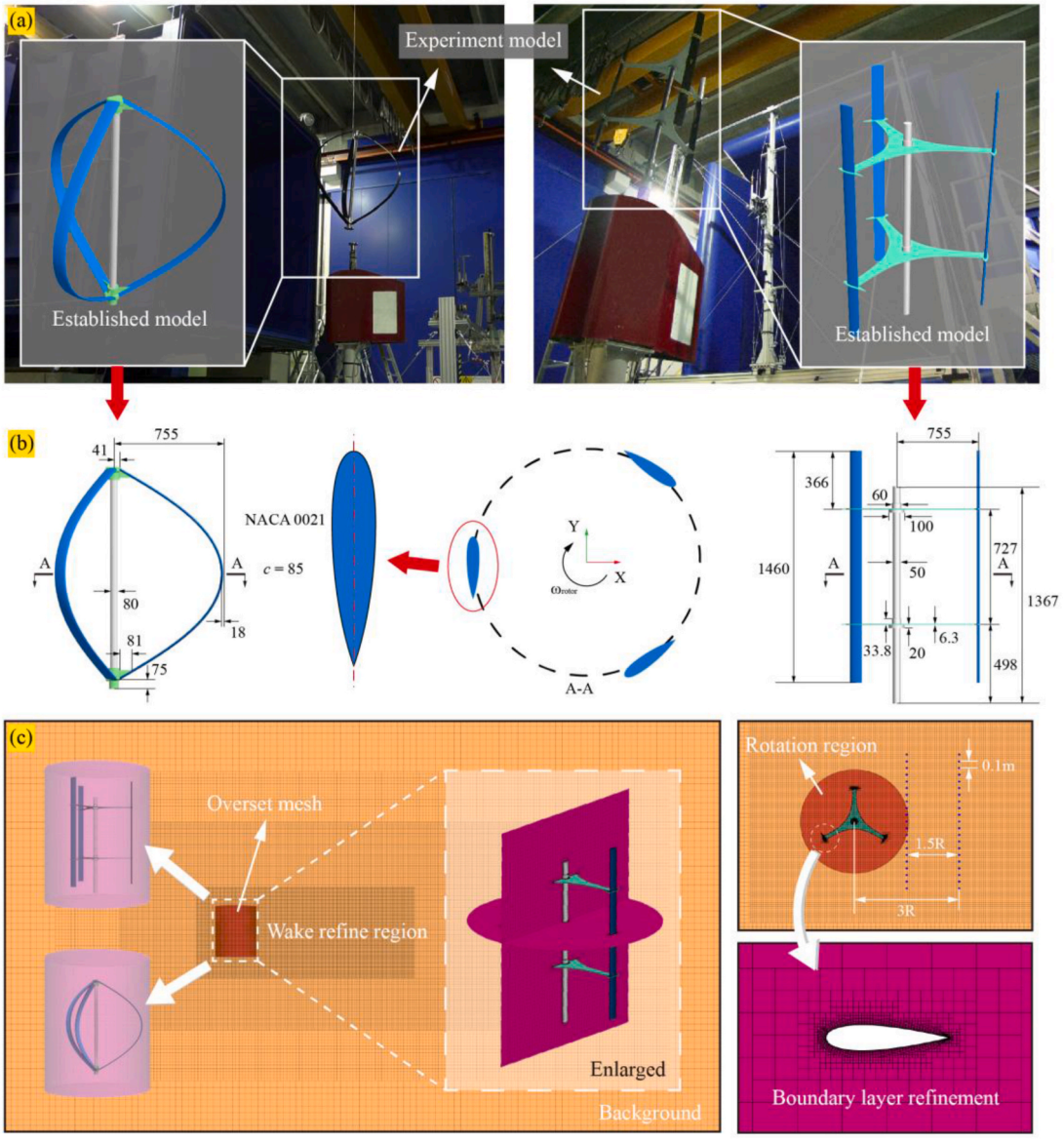


Fig. 10. Wind tunnel model and the corresponding numerical setup of the H-type and Φ-type VAWTs: (a) wind tunnel test model; (b) computational geometric model; (c) mesh and boundary conditions.

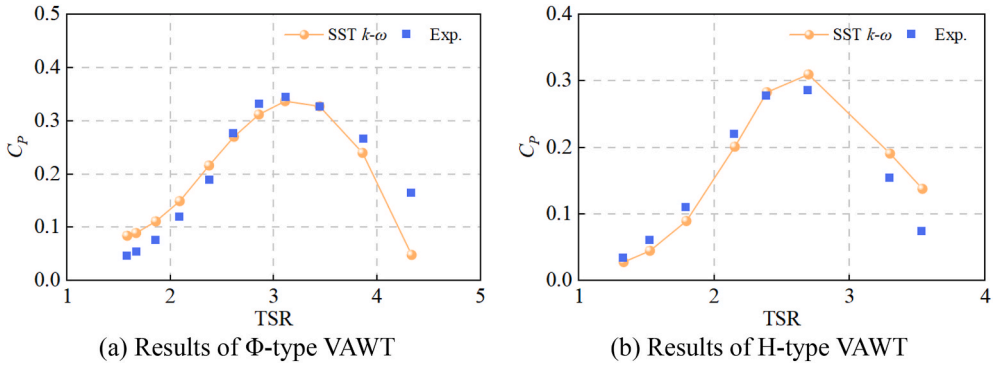


Fig. 11. Comparison of experimental and simulated power coefficients of the two VAWTs at different TSRs.

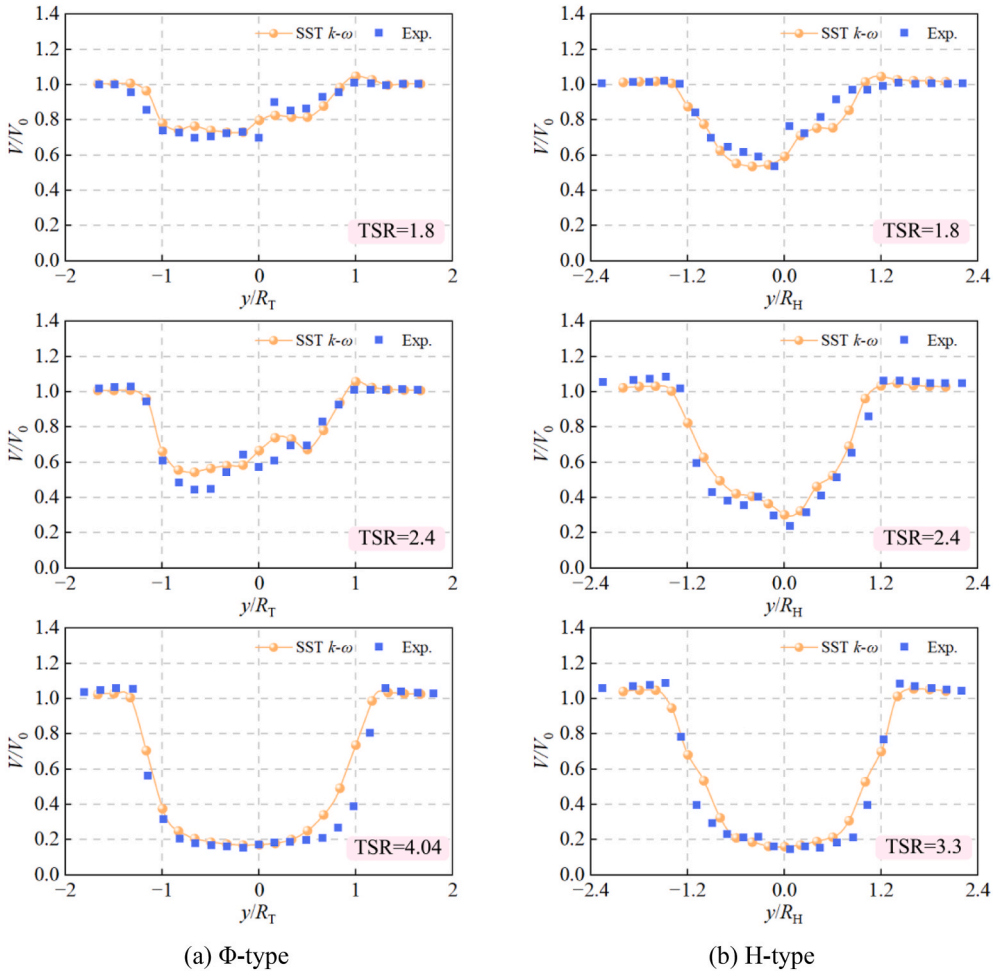


Fig. 12. Comparison of experimental and simulated wake velocities of the two VAWTs at different TSRs.

sensitivity study was not conducted in this work. Therefore, the present validation mainly supports the suitability of the SST *k-ω* model for the time-averaged aerodynamic performance and wake field considered in this study. Since the URANS-based SST *k-ω* model resolves the averaged effect of turbulence, some instantaneous vortex structures and small-scale turbulent fluctuations may not be fully captured. Overall, the SST *k-ω* model provides a reasonable balance between prediction accuracy and computational cost for the present full-scale coupled simulations.

4.3. Hydrodynamic validation

The free decay test involves applying an initial displacement or rotational angle to the platform and then releasing it to measure the free vibration decay process in still water, thereby obtaining key hydrodynamic parameters such as natural frequency and damping. Since aerodynamic loads are not considered in this scenario, the modeling of the blades is neglected in this study, and they are treated as an equivalent mass concentrated at the nacelle location to ensure that the system mass and moment of inertia are consistent with the original design (Fig. 13). The platform's main parameters are listed in Table 7. The initial

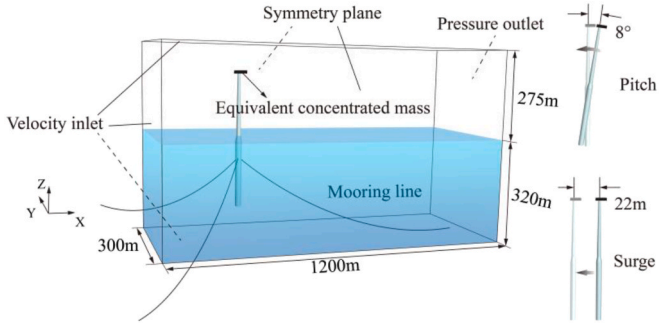


Fig. 13. Free decay validation model of OC3 Spar platform.

conditions for the simulation are set as a longitudinal displacement of 22 m and a pitch angle of 8°, after which the platform is released, and its free decay response is computed (see Fig. 14).

In this study, the free decay results of the Spar platform are calculated using the CFD method and compared with other numerical methods [47]. Fig. 14 (a) presents the computed sway response. The CFD method shows good agreement with the FAST program, but there are some discrepancies in the logarithmic decay rate when compared to the ADAMS and HAWC2 programs. Fig. 14 (b) shows the computed pitch response, indicating that the CFD method is in high agreement with the ADAMS results. However, over time, the differences between CFD and the HAWC2 and FAST programs gradually increase. Since the CFD method accounts for the viscous effects of the fluid, some differences with other methods are observed, but all results fall within a reasonable range, thereby validating the reliability of the CFD method used.

5. Results and discussion

To determine the appropriate Tip Speed Ratio (TSR) range and select the optimal operating conditions for subsequent formal simulations, the variation of power coefficients for both VAWT configurations at different TSRs was calculated by adjusting the inlet wind speed (ranging from 6 to 10 m/s) in the preliminary parameter exploration stage, with the results presented in Fig. 15. Notably, this varying inlet velocity is used only for preliminary parameter analysis (to obtain different TSR responses and select optimal conditions) rather than formal simulation boundary conditions; all formal calculations in this paper use a fixed inlet wind speed of 8 m/s to ensure comparability between the two configurations. It can be observed from Fig. 15 that the power coefficient trends for both VAWT types generally follow a similar pattern, with the Φ-type VAWT exhibiting a relatively higher power coefficient, indicating its superior ability to capture wind energy. Further comparison reveals that the optimal TSR for both VAWTs lies within the range corresponding to the 8-9 m/s incoming wind speed, further verifying the rationality of selecting 8 m/s as the fixed inlet wind speed for formal simulations.

5.1. Aerodynamic performance

5.1.1. Characteristics of aerodynamic loads

Fig. 16 presents a comparison of the power coefficients (C_P) for both VAWT types. From Fig. 16(a), it can be observed that the time-averaged power coefficient is 0.378 for the Φ-type VAWT and 0.201 for the H-type VAWT, suggesting a notable aerodynamic efficiency advantage of the Φ-type rotor. This is due to the shorter support structure of the Φ-type VAWT, which causes less interference to the airflow, allowing it to flow more smoothly over the blades. This reduces energy losses and increases power output. In contrast, the longer support structure of the H-type VAWT creates a greater obstruction to the airflow, leading to significant blockage effects, which in turn cause increased flow disturbances and energy losses, resulting in a reduction in power output. Fig. 16 (b) shows a local magnification of the C_P in the 1500-1560 s range. It can be seen that the C_P response exhibits both high-frequency and low-frequency fluctuations. The high-frequency component coincides with the blade passing frequency and is caused by the periodic changes in relative inflow velocity and angle of attack as the blade rotates through different azimuths, leading to aerodynamic load fluctuations. The low-frequency component coincides with the wave period and is induced by platform motion, which further alters the blade's relative inflow conditions.

Table 7
Main parameters of the platform.

Properties	Value
Gross mass	8.06×10^6 kg
Centroid position below static water level	78.04 m
Rolling inertia	2.0×10^{10} kg m^2
Pitching inertia	2.0×10^{10} kg m^2
Yawing inertia	1.6×10^{10} kg m^2

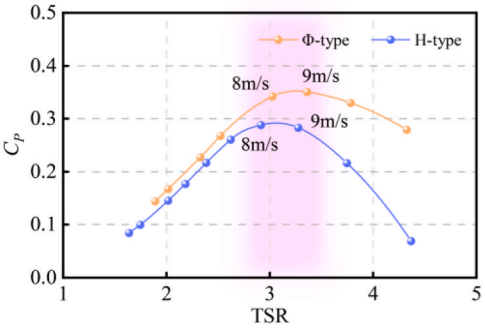


Fig. 15. Variation of C_P with TSR for the two VAWTs.

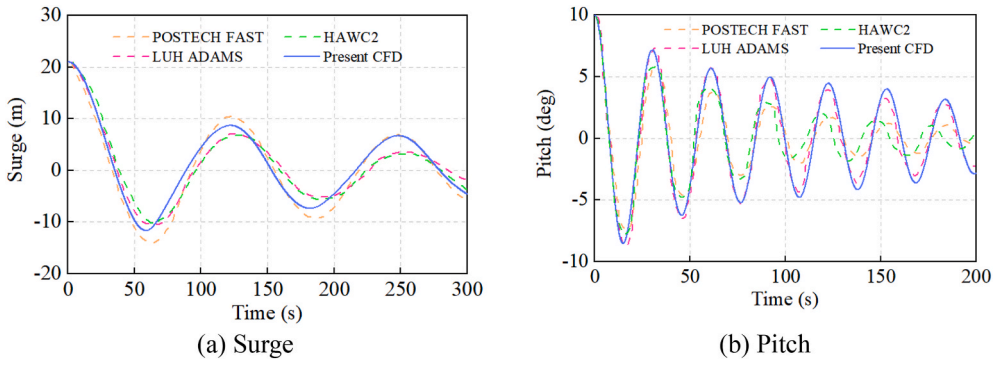
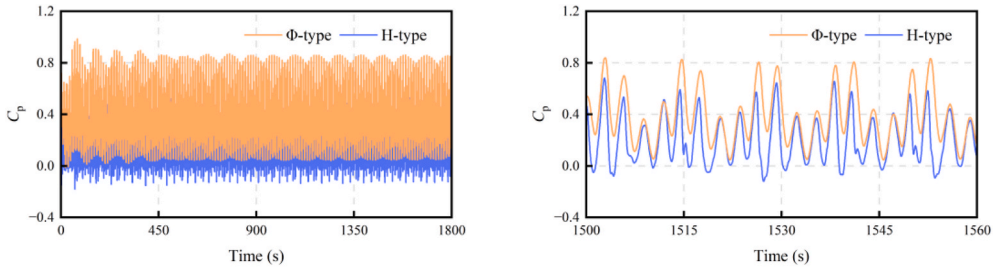


Fig. 14. Free-decay validation results.



(a) Power comparison (b) Detail amplification

Fig. 16. Power coefficient comparison of two VAWTs.

Additionally, it can be observed that the power coefficient reaches negative values at certain moments. This is due to the platform's pitch and sway motion, which at specific times weakens the rotor's relative inflow wind speed, causing the instantaneous angle of attack to deviate from the effective lift-producing range, thus generating an instantaneous negative aerodynamic torque.

Fig. 17 illustrates the differences in the thrust coefficients of the two VAWT types. Unlike the power coefficient, the overall trend shows that the time-averaged thrust coefficient is 0.811 for the H-type VAWT and 0.744 for the Φ-type VAWT, meaning that the thrust coefficient of the H-type rotor is approximately 9% higher. Although both have the same rotational angular velocity, the H-type VAWT has a larger projected area of the support structure, which results in a stronger obstruction to the incoming flow, thereby generating a larger thrust.

To analyze the aerodynamic performance differences of the blade configurations, Fig. 18 presents a comparison of the net torque output of the blades for the two types of VAWTs. As shown in the figure, the torque response exhibits two distinct output regions: the upstream region with an azimuth angle in the range of 0-180° and the downstream region with an azimuth angle in the range of 180-360°. When the blade operates in the upstream region, the relative inflow speed is maximal, and the blade is within the optimal angle of attack range, resulting in a larger aerodynamic force and higher torque peaks. In the downstream region, the blade is in the lee side, where the relative inflow speed weakens, causing a decrease in the aerodynamic loads on the blade. Additionally, the changes in the angle of attack exacerbate flow separation and dynamic stall, leading to a smoother torque variation. From the comparison, it can be seen that in the upstream region, the torque of the H-type VAWT is higher than that of the Φ-type VAWT. This is because in the H-type VAWT, the blades at different heights all operate at the same radius, so the aerodynamic forces at each position are converted into torque with the maximum lever arm. In contrast, the Φ-type VAWT has blades at different radii at different heights, with the maximum occurring only at the equatorial plane, which results in a lower overall torque compared to the H-type VAWT. In the downstream region, the torque output of the H-type VAWT is less stable than that of the Φ-type VAWT. This is due to strong wake interference downstream, which destabilizes the flow field and prevents the blade from obtaining a stable aerodynamic force to convert into torque when it enters the downstream region.

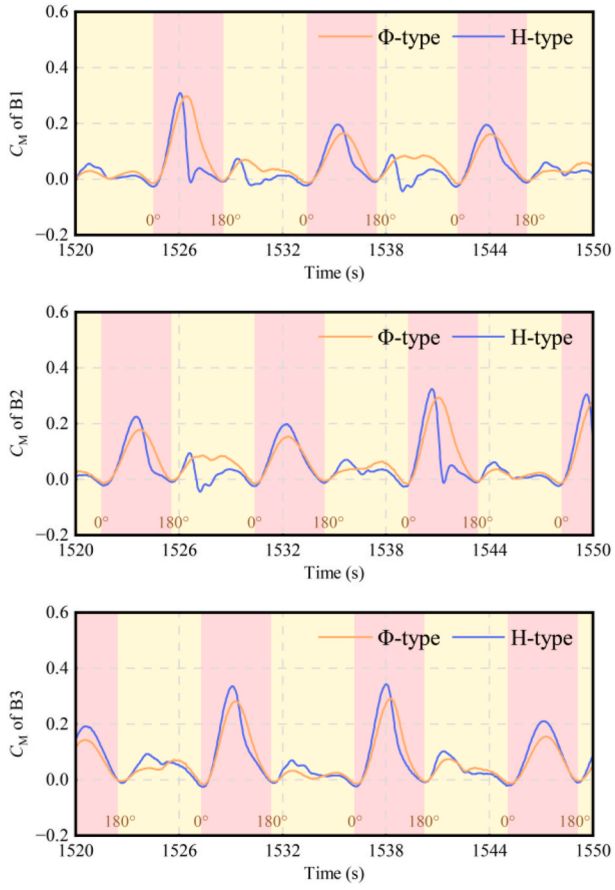
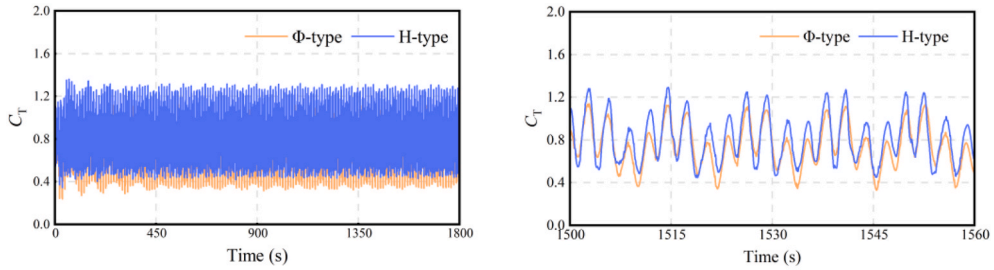


Fig. 18. Torque coefficient comparison of the two VAWTs.



(a) Thrust comparison (b) Detail amplification

Fig. 17. Thrust coefficient comparison of two VAWTs.

To further explain the aerodynamic mechanism of torque generation, Fig. 19 presents the torque coefficient of blade B1 together with the pressure distributions at representative azimuthal positions over one rotation cycle. The blade torque is mainly governed by the pressure difference between the two sides of the blade and the resulting tangential force component. Near 0° and 180°, the pressure distribution around B1 is relatively symmetric, corresponding to the low torque values in the curve. In the upwind region, the pressure difference across the blade increases and produces the main positive torque contribution. Around 90°, the Φ-type blade shows a stronger pressure contrast between the pressure side and suction side, which agrees with its higher torque coefficient at this azimuth. By contrast, the H-type blade reaches its positive torque peak earlier but decreases rapidly after approaching 90°, indicating a shorter effective torque-producing range. In the downwind region, the pressure difference across the blade becomes smaller, and the corresponding torque contribution remains low or may become negative. This comparison shows that the Φ-type rotor can maintain a more effective pressure difference over a wider azimuthal range, while the H-type rotor exhibits a sharper and narrower positive-torque response.

Fig. 20 shows the variations of C_l, C_d, and angle of attack α of blade B1 at different spanwise positions. For the Φ-type rotor, the aerodynamic coefficients show stronger spanwise variation because the curved blade geometry changes the local relative inflow along the blade height. In contrast, the H-type rotor exhibits more similar trends among P1, P2, and P3 due to its straight blade geometry. For both configurations, the main positive lift occurs in the upstream half of the rotation, where the angle of attack remains within an effective lift-producing range. In the downstream half, the angle of attack changes rapidly and the drag coefficient increases locally, indicating stronger flow separation and unsteady aerodynamic loading. These coefficient variations are consistent with the pressure distribution shown in Fig. 19 and are further supported by the flow-field and Q-criterion vortex structures in Fig. 23, where vortex shedding and separated flow become more evident in the wake-affected region.

5.1.2. Velocity deficit

Velocity deficit reflects the wake recovery characteristics and the downstream energy loss of the turbine. Fig. 21 shows the velocity distribution along the Y-direction at different distances downstream of the rotor for the Φ-type and H-type VAWTs. From the figure, it can be observed that the velocity distribution in the Y-direction at different downstream distances follows a generally consistent pattern: the velocity is lowest directly behind the rotor (at Y/D = 0); as the distance from the rotor center increases, the velocity gradually recovers to the incoming wind speed. The key difference between the two is that, compared to the Φ-type VAWT, the H-type VAWT experiences a lower overall velocity deficit. As the wake area expands, the turbulence in the wake gradually mixes with the surrounding free-flowing fluid, causing the velocity to recover, thereby reducing the velocity deficit. In summary, the H-type VAWT exhibits lower velocity deficit in the wake region and a faster recovery of the wake compared to the Φ-type VAWT. This has a positive impact on wind farm layout because lower velocity deficit and faster wake recovery can reduce the impact of the wake on downstream turbines, helping optimize the overall performance of the wind farm.

5.1.3. Flow field analysis

Flow field analysis is conducted to further explain the wake evolution and aerodynamic differences between the two rotor configurations. Fig. 22 compares the downstream vortex distribution of the Φ-type and H-type VAWTs at different streamwise locations. In the YZ sections, both wakes experience formation, development, diffusion, and attenuation as they propagate downstream. At X/D = 1, distinct vortex concentration regions can be observed behind both rotors. The Φ-type rotor presents a relatively continuous vortex distribution along the outer wake boundary, while the H-type rotor shows a more irregular vortex pattern near the blade-swept region. This difference is mainly related to their blade-end and support layouts. The closed blade-end connection of the Φ-type rotor reduces free tip-vortex shedding and helps maintain a more coherent wake structure. In contrast, the open blade tips and horizontal

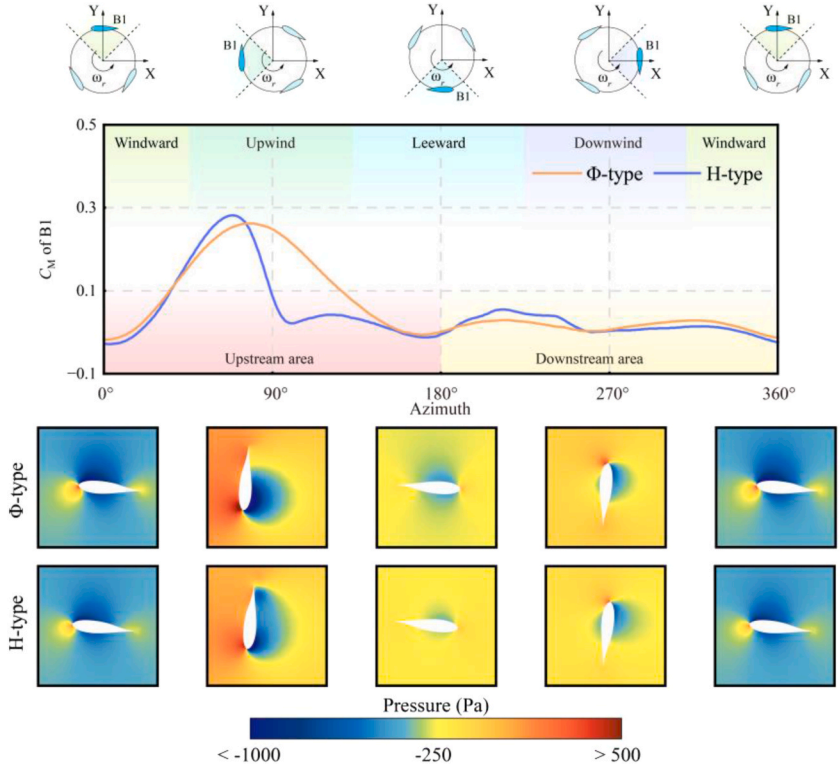


Fig. 19. Torque coefficient of blade B1 and pressure fields around blade B1 at representative azimuthal positions.

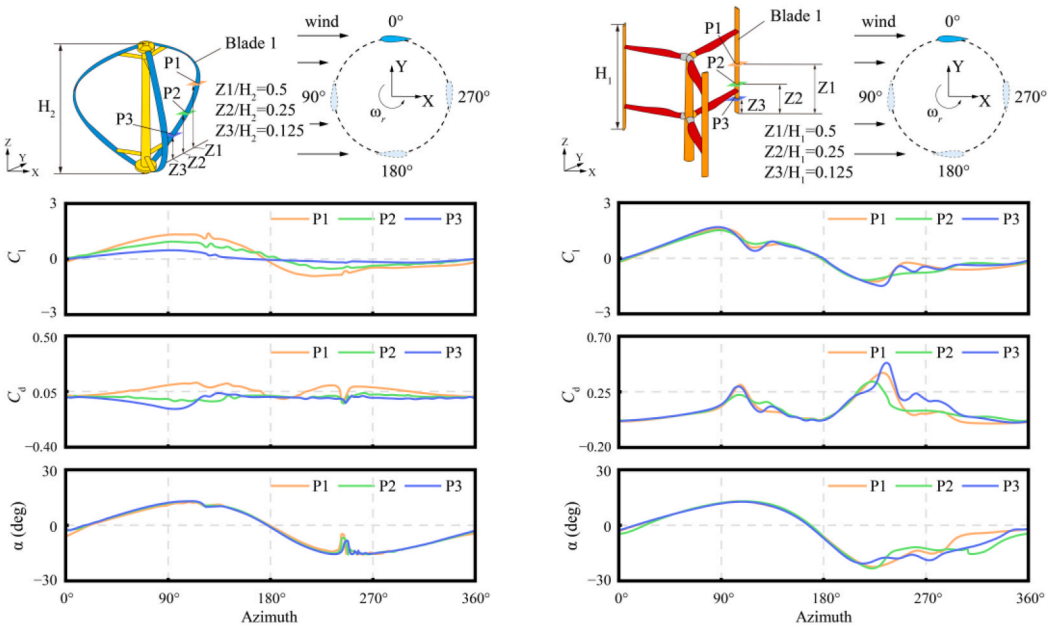


Fig. 20. Variations of C_l, C_d and α with azimuth angle at different spanwise positions of Blade 1 for two VAWTs.

support arms of the H-type rotor introduce stronger local disturbances, leading to a more scattered wake field.

As the wake develops downstream, the difference between the two configurations becomes clearer. In the range of $2 \leq X/D \leq 3$, the Φ-type wake still contains larger coherent vortex structures, whereas the H-type wake shows stronger diffusion and more secondary vortices. At $4 \leq X/D \leq 5$, the Φ-type wake retains more visible coherent vortex cores and a stronger velocity deficit, indicating slower wake recovery. By contrast, the H-type wake becomes more dispersed, suggesting stronger mixing with the surrounding flow and faster wake recovery. This is consistent with the velocity deficit analysis in Fig. 21, where the H-type rotor shows a lower downstream velocity deficit. The XZ-plane distributions further show that the Φ-type wake mainly develops along the outer boundary of the rotor-swept region, leaving a relatively low-vorticity region near the wake center. For the H-type rotor, the wake is more widely distributed across the downstream region, which is associated with the disturbance induced by the horizontal support arms and open blade tips. These wake characteristics are consistent with the aerodynamic results discussed above. The Φ-type rotor achieves higher power output because of lower support-induced flow losses and a more sustained torque-producing process, while the H-type rotor promotes stronger wake mixing and faster recovery at the cost of larger aerodynamic disturbances and lower power coefficient.

Fig. 23 compares the instantaneous flow fields of the Φ-type and H-type VAWTs at different phases within one wave period. The velocity contours on the XZ and XY sections show the wake velocity distribution, while the Q-criterion is used to identify the main three-dimensional vortex structures, as expressed in Eq. (22).

$$Q = \frac{1}{2}\left(\|\omega\|^2 - \|S\|^2\right) \tag{22}$$

In the equation, ω represents the rotation rate tensor, i.e., the vorticity, and S is the strain rate tensor. When $Q > 0$, it indicates the presence of vortex structures in the flow field, with the rotational component of the fluid being dominant. When $Q < 0$, it indicates that the strain rate component dominates the flow field. Clear differences can be observed between the two rotor configurations. For the H-type VAWT, the open blade tips and horizontal support arms generate more discrete vortical structures near the rotor and in the near wake. These structures are convected downstream and contribute to stronger wake disturbance and lateral diffusion. By contrast, the Φ-type VAWT does not show the same tip-vortex pattern because of its closed blade-end connection. Its vortical structures are more closely distributed along the curved blade path and the closed blade boundary, leading to a more continuous wake development. This difference is consistent with the wake behavior shown in Fig. 22, where the H-type wake exhibits stronger diffusion, whereas the Φ-type wake remains more coherent during downstream propagation.

The flow-field features in Fig. 23 also help explain the local aerodynamic coefficient variations shown in Fig. 20. For the H-type rotor, the straight blade geometry leads to relatively similar C_l, C_d, and angle-of-attack variations at different spanwise positions, but stronger local fluctuations appear when the blade passes through the wake-affected region. These fluctuations correspond to the more fragmented vortical structures and disturbed near-wake flow shown in Fig. 23(e)–(h). For the Φ-type rotor, the curved blade geometry causes more evident spanwise differences in C_l, C_d, and α, as shown in Fig. 20(a). This is consistent with the non-uniform local flow along the curved blade and the more distributed vortical structures observed in Fig. 23(a)–(d). Therefore, the combined analysis of Figs. 20 and 23 indicates that the two rotor configurations differ not only in global wake development, but also in the spanwise distribution of local aerodynamic loading and unsteady flow structures.

5.2. Hydrodynamic performance

5.2.1. 6-DOF response analysis

The floating platform motion is solved using the DFBI 6-DOF rigid body model, including three translational and three rotational degrees of freedom. Rotor rotation is realized using the overset mesh method with a prescribed rotational speed. The rotor region follows the 6-DOF motion of the floating platform and simultaneously rotates around the vertical axis. Therefore, the rotor rotation is independent of the inlet wind speed, while the coupled response of the floating system is determined by aerodynamic loads, hydrodynamic loads, gravity, buoyancy, and mooring restoring forces. The 6-DOF responses for the two types of VAWT are shown in Fig. 24. It can be observed that the heave, sway, and pitch responses (Fig. 24(a)–(c)) exhibit similar characteristics, that is,

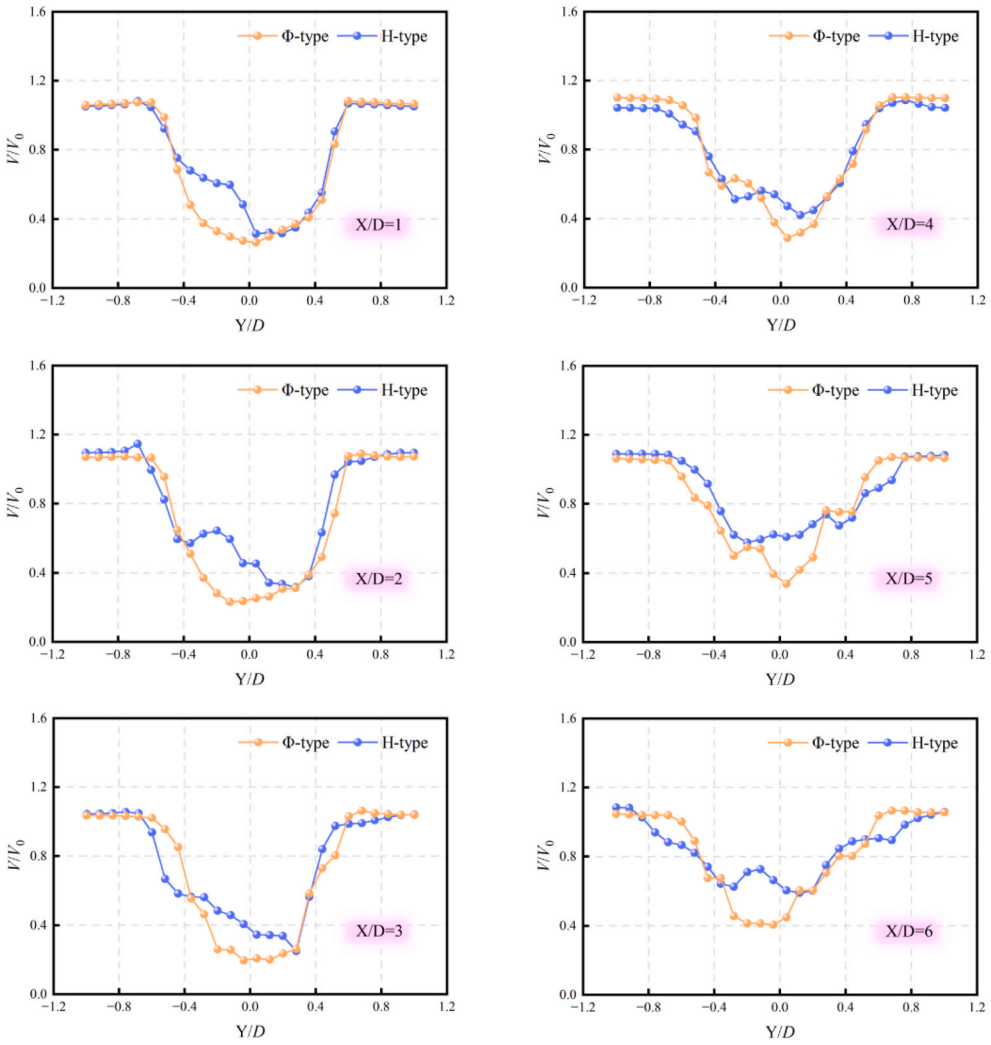


Fig. 21. Velocity distribution of the two VAWTs at different downstream distances.

the superposition of small-period wave motions and large-period slow drift motions. Over time, the slow drift motion stabilizes. The slow drift phenomenon is the low-frequency drift induced by long-period wave excitation forces, primarily caused by the coupling effect between the platform's natural frequency and the wave frequency. Especially under the influence of long-period waves, the platform's responses in the heave, pitch, and sway degrees of freedom gradually accumulate, leading to large displacements. However, as time progresses, the platform's motion amplitude gradually decreases, eventually stabilizing due to the combined effects of the system's damping, hydrodynamic restoring forces, and mooring restoring forces.

On the other hand, the sway and roll responses of the two types of VAWT (Fig. 24(d) and (e)) exhibit similar overall trends. In the initial stage, the amplitude gradually increases, and then stabilizes in the middle and later stages, showing periodic oscillations primarily driven by the wave period, with some low-frequency components superimposed. The sway is mainly influenced by the first-order wave forces and low-frequency drift forces. Initially, the sway amplitude increases gradually over time. In the middle and later stages, as the hydrodynamic damping and restoring forces from the mooring system begin to take effect, the lateral displacement is constrained from further increasing, eventually bringing the system into a dynamic equilibrium state. The roll response is significantly affected by not only the wave-excitation moment but also the restoring moment from the mooring system and the aerodynamic loads on the blades. Due to transient excitation, the roll response has a larger amplitude in the initial stage. Over time, the hydrodynamic damping and restoring moments dissipate the system's energy, leading to a rapid attenuation of the roll response, which then settles into small-amplitude oscillations primarily at the wave frequency.

The pitch (Fig. 24(f)) response exhibits a more stable and long-lasting periodic oscillation, with the oscillation period primarily determined by the natural period of the floating body. Since the excitation source for pitch is the horizontal moment, the effects of wave periods and aerodynamic loads on the blades are minimal, causing the pitch response to exhibit more independent periodic oscillatory characteristics. Compared to roll, the decay trend of pitch is less pronounced, and the oscillation is more persistent. The restoring moment for pitch mainly comes from the mooring system's pitch restoring stiffness. Under the combined effects of wind and wave, the platform experiences alternating horizontal moments, leading to a long-lasting yaw oscillation. Unlike roll, pitch is usually not strongly constrained by fluid damping and dissipates energy more slowly, making it easier to maintain a stable periodic oscillation. Meanwhile, the rotation of the VAWT rotor generates a gyroscopic effect, and the restoring moment caused by this effect partially intensifies the platform's pitch response.

To further compare the 6-DOF response differences between the two types of VAWTs, data from 1400 to 1800s were selected for further analysis, and the results are shown in Table 8. It can be seen that the pitch and heave equilibrium positions of the H-type VAWT are higher

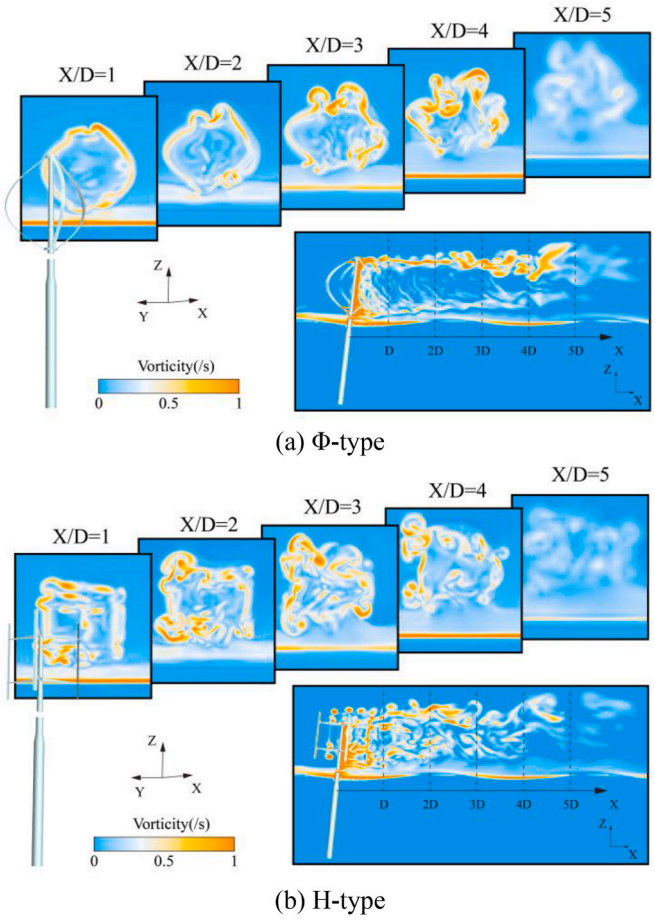


Fig. 22. Comparison of downstream wake distribution of two types of VAWT.

than those of the Φ-type VAWT. This is mainly due to its more complex support structure, which increases its relative windward area. Consequently, the aerodynamic thrust it receives is also greater, causing the heave equilibrium position to deviate farther downstream. This results in a larger horizontal mooring force and a corresponding increase in the vertical mooring force, ultimately leading to the heave equilibrium position being farther from Φ-type VAWT. For the roll response, the equilibrium position of the Φ-type VAWT is higher than that of the H-type VAWT. This is because the heave and sway equilibrium positions of the Φ-type VAWT are smaller, leading to a reduction in the mooring restoring moment. Significant differences are observed in the sway and yaw responses due to the differing hydrodynamic, aerodynamic, and coupling mechanisms between the two types of VAWTs. The pitch response for both VAWT types is mainly influenced by their inherent natural period and does not show significant external excitation differences. Moreover, the standard deviations of the two types of VAWTs are quite similar. Overall, the Φ-type VAWT exhibits better overall stability compared to the H-type VAWT.

5.2.2. Mooring lines tension

The analysis of mooring tension is crucial for evaluating the stability and safety margin of the wind turbine platform in offshore environments. Fig. 25 compares the mooring tension responses of the two VAWTs. Overall, the three mooring lines show clear transient oscillations in the initial stage and then gradually reach a quasi-periodic steady state. This trend is consistent with the platform motion response discussed in Section 5.2.1, indicating that the mooring loads are mainly governed by the coupled platform motions and mooring restoring forces. For M1, the mean tensions of the two configurations are almost identical, with average values of 0.973×10^6 N for the Φ-type VAWT and 0.972×10^6 N for the H-type VAWT. The tension amplitudes are also very close. This is because M1 is mainly affected by the surge response, and the two configurations show only a very small difference in the stabilized surge motion. For M2, the Φ-type VAWT shows a slightly higher mean tension than the H-type VAWT, with average values of 1.154×10^6 N and 1.143×10^6 N, respectively. In contrast, for M3, the H-type VAWT produces a higher mean tension of 1.171×10^6 N, compared with 1.143×10^6 N for the Φ-type VAWT. The different trends of M2 and M3 are mainly related to the sway response. As shown in Fig. 24(d), the Φ-type VAWT exhibits a larger sway offset than the H-type VAWT. Since M2 and M3 are symmetrically arranged with respect to the X-axis, this lateral offset directly changes the stretching state of the two mooring lines. The larger sway offset of the Φ-type VAWT tends to increase the tension in M2, while the symmetric mooring line M3 becomes relatively relaxed. As a result, the mean tension of M2 is higher for the Φ-type VAWT, whereas the mean tension of M3 is higher for the H-type VAWT. This indicates that rotor configuration mainly affects the redistribution of mooring tension through the coupled surge-sway platform motion, rather than causing a uniform increase or decrease in all mooring lines.

5.3. Power spectral density

Power spectral density (PSD) analysis is used to identify the dominant frequency components of the aerodynamic and platform dynamic responses of the floating VAWTs. In this study, the initial transient stage was excluded, and the response signals from 10.0 s to 1800.0 s were used. The sampling interval was 0.02 s, corresponding to a sampling frequency of 50 Hz. The PSD was calculated using the built-in Power Spectral Density data set function in STAR-CCM+. One analysis block with zero overlap was used, and no additional window function or filter was applied. The spectra are reported as PSD values of the original response variables without additional normalization. Since the main characteristic frequencies are concentrated in the low-frequency range, the PSD results are presented within 0 to 1 Hz. Fig. 26 presents the PSD comparison of the power coefficient time series for the two VAWTs. The main characteristic frequencies in the power coefficient response include the first-order wave frequency f_w, wave harmonic frequencies, the blade-passing frequency f_b, and its harmonics. The wave-frequency components indicate that wave-induced platform motions affect the relative inflow and angle of attack of the rotor, thereby modulating the aerodynamic power. The blade-passing frequency is associated with the periodic variation of aerodynamic loading as the blades rotate through different azimuthal positions.

In the low-frequency region, both VAWTs show a clear peak at the first-order wave frequency of 0.08268 Hz, indicating that the power coefficient is modulated by wave-induced platform motion. Several peaks also appear at wave harmonic frequencies, suggesting nonlinear interactions among wave excitation, platform motion, and aerodynamic loading. In addition, the blade-passing frequency at 0.34022 Hz is clearly observed in both spectra, reflecting the periodic aerodynamic response caused by rotor rotation. Compared with the Φ-type VAWT, the H-type VAWT shows higher PSD energy near the blade-passing frequency and its high-frequency components. This is physically related to its open blade tips and the two horizontal support arms connecting the blades to the central shaft. The open blade tips promote tip-vortex shedding and three-dimensional flow separation, while the horizontal support arms introduce additional blockage, vortex shedding, and periodic drag fluctuations. These effects interact with dynamic stall on the straight blades and amplify the unsteady aerodynamic response. In contrast, the Φ-type rotor has closed blade-end connections and root-concentrated supports, which reduce free tip-vortex formation and support-induced disturbances. As a result, the Φ-type rotor shows weaker high-frequency PSD energy in the power coefficient response. From an engineering perspective, the PSD of the power coefficient helps identify the dominant sources of aerodynamic power fluctuation. Strong

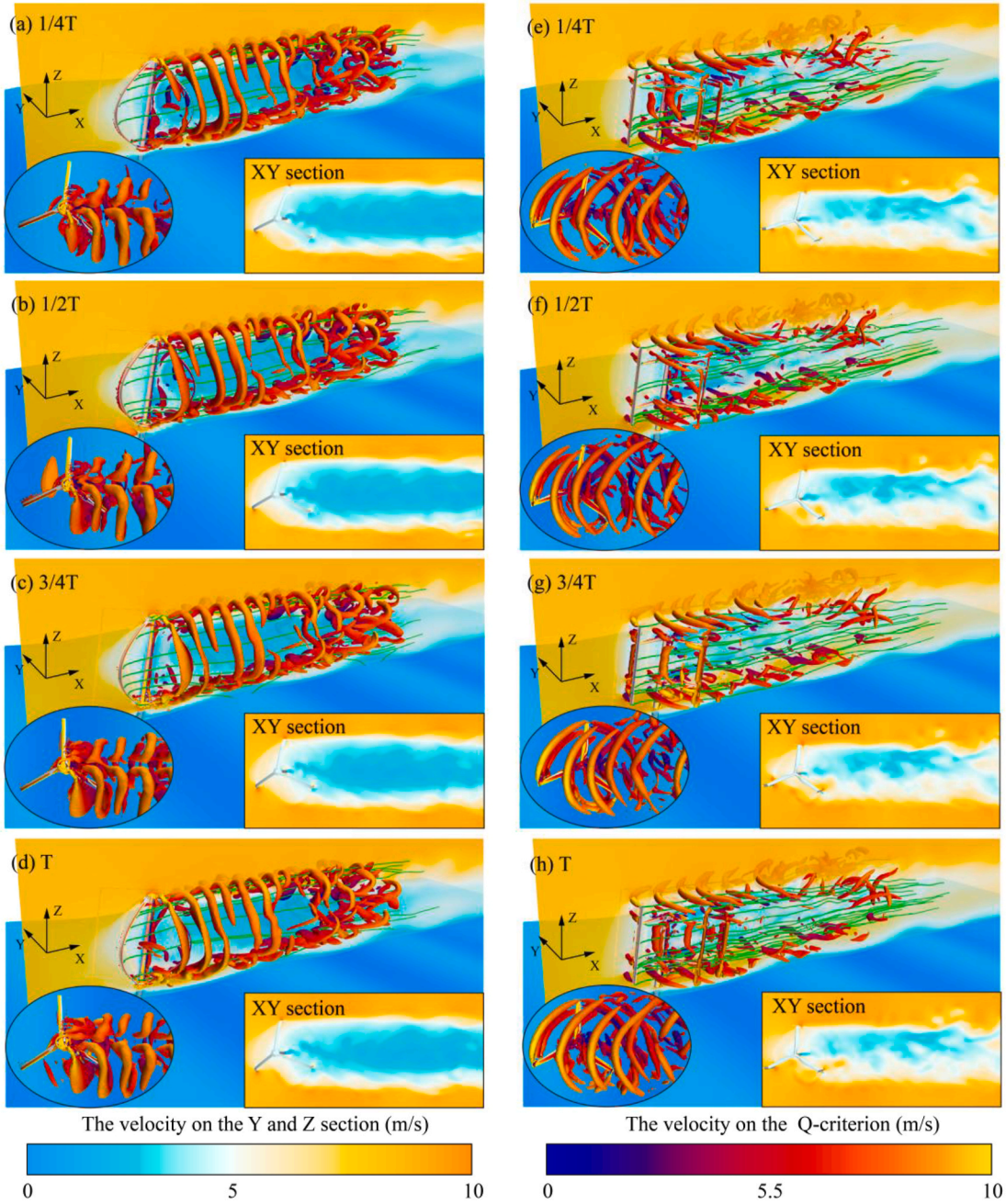


Fig. 23. Comparison of flow field distribution of two types of VAWT at different times.

peaks near the wave frequency indicate platform-motion-induced power modulation, while peaks near the blade-passing frequency reflect periodic aerodynamic loading. Lower PSD amplitudes at these frequencies imply weaker power and load fluctuations, which is beneficial for smoother energy conversion and reduced fatigue excitation. Therefore, the spectral characteristics of the power coefficient can support rotor configuration selection and coupled floating system design.

Fig. 27 presents the PSD results of the 6-DOF responses for the two VAWTs. The symbols f_H and f_Φ represent the natural frequencies of the H-type and Φ-type floating systems for the corresponding degrees of freedom, respectively. Compared with the PSD of the power coefficient, the 6-DOF responses show more concentrated spectral energy, mainly around the platform natural frequencies, the first-order wave frequencies, wave harmonic frequencies, and blade-passing frequencies. For the heave and surge responses shown in Fig. 27(a) and (b), the energy is mainly concentrated in the low-frequency region, while the surge response is strongly affected by low-frequency drift, with additional contributions from the wave frequency and its harmonics. For the pitch and sway responses in Fig. 27(c) and (d), peaks appear near the natural frequencies, the first-order wave frequency, and the blade-passing frequency, indicating that rotor-induced periodic aerodynamic loads are transmitted to platform motions through the coupled aero-hydro-mooring system. For the roll and yaw responses in Fig. 27(e) and (f), significant energy peaks are observed at higher-order wave frequencies, and the PSD curves for both VAWTs show noticeable separation. This indicates that higher-order harmonics of the waves have a significant impact on the platform's dynamic response. Additionally, in the yaw response, the H-type VAWT exhibits more peak values at different frequencies compared to the Φ-type VAWT. These peaks correspond to higher-order wave harmonics and rotor-induced aerodynamic fluctuations of the H-type VAWT. Overall, the energy of the responses for each degree of freedom is mainly concentrated in the low-frequency region,

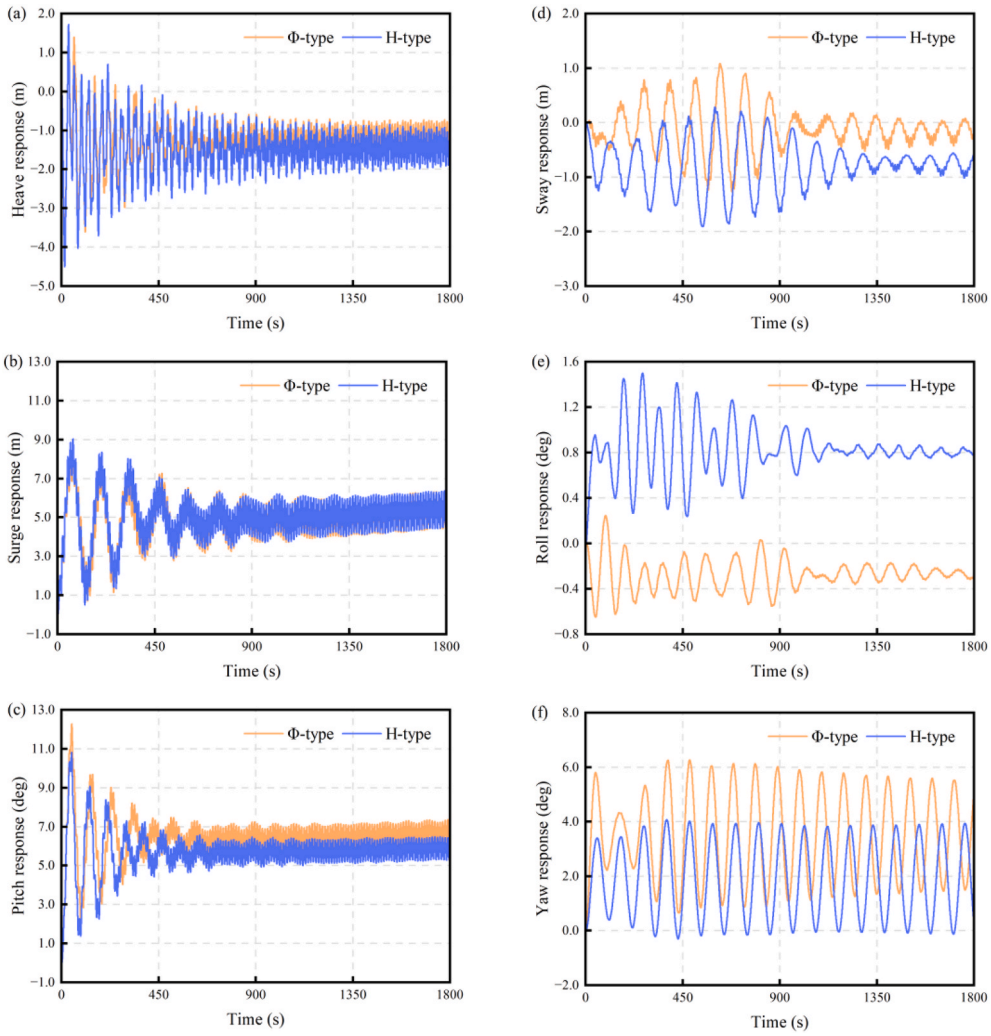


Fig. 24. The 6-DOF comparison of two VAWTs.

Table 8
Comparison of 6-DOF results of two VAWTs.

6-DOF	Φ-type		H-type	
	Average value	Standard deviation	Average value	Standard deviation
Heave [m]	−1.293	0.324	−1.438	0.329
Surge [m]	5.280	0.674	5.303	0.671
Pitch [°]	6.672	0.414	5.849	0.412
Sway [m]	−0.153	0.146	−0.752	0.120
Roll [°]	−0.263	0.041	0.803	0.030
Yaw [°]	3.499	1.444	1.986	1.401

with the frequency domain characteristics being primarily governed by the system's natural frequencies, the first-order wave frequency, and its higher-order harmonics. The energy in the high-frequency region exhibits a significant attenuation trend as the frequency increases, indicating that the platform's dynamic response is controlled by a limited set of characteristic frequencies.

6. Conclusions

To address the existing research gaps in the comparative evaluation of floating VAWT configurations and their coupled dynamic mechanisms, and to provide a transferable basis for configuration selection, site layout, and engineering design of deep-water floating VAWTs, this study conducts high-fidelity, fully coupled, and systematic simulations of Φ-type and H-type VAWTs with identical swept areas. Using CFD methods combined with the DFBI module and a VOF-based wave model, the study systematically compares and analyzes their aerodynamic loads, wake velocity and flow-field characteristics, 6-DOF responses, and mooring line tensions in a wind-wave coupled environment. The main conclusions are as follows:

(1) The H-type VAWT, due to its larger spanwise support structure, induces significant blockage effects and associated flow losses. Additionally, the tip vortices generated at the blade tips induce additional three-dimensional flow losses, further reducing its overall aerodynamic efficiency. In contrast, the Φ-type VAWT adopts a closed blade structure with less spanwise supporting interference, which weakens the blockage effect and reduces additional flow losses.

(2) Benefiting from the straight blade geometry, the H-type VAWT achieves higher instantaneous blade torque in the upstream region. However, the extended support structure induces significant flow disturbances, leading to a relatively reduced torque stability in the downstream region compared with the Φ-type configuration. Additionally, the Φ-type VAWT exhibits more evident spanwise variations in C_l, C_d and α, reflecting the influence of its curved blade geometry on local aerodynamic loading.

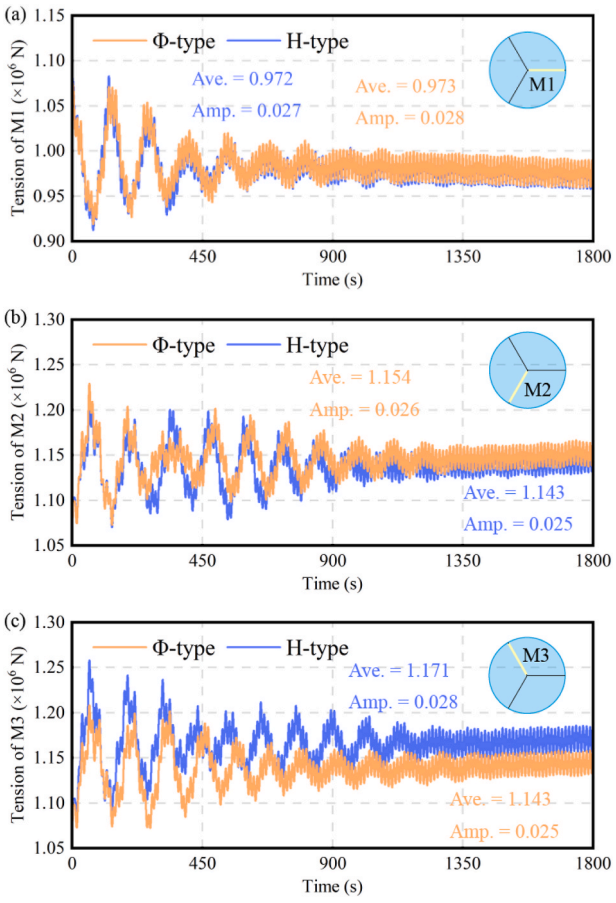


Fig. 25. Comparison of mooring tensions between the two VAWTs.

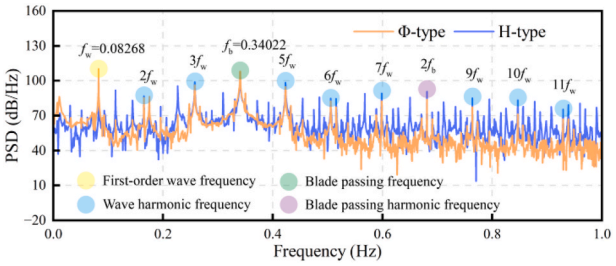


Fig. 26. PSD comparison of power coefficients of the two VAWTs.

(3) The H-type VAWT exhibits smaller velocity deficit and faster wake recovery. This behavior is due to its complex support structure and tip-vortex interactions, which intensify turbulence and secondary vortex formation, thus promoting momentum exchange and wake recovery. This characteristic has a positive impact on wind farm layout. However, this intensified mixing leads to higher energy losses and even the occurrence of negative aerodynamic torque. In contrast, the Φ-type VAWT's wake displays a more coherent wake with fewer vortical structures, thus resulting in lower energy loss and higher power output. However, this also somewhat inhibits radial mixing, delaying the wake recovery process.

(4) The larger support structure of the H-type VAWT leads to a greater windward projected area and higher thrust resulting in slightly larger downstream surge drift and a redistribution of mooring tensions. Additionally, the H-type VAWT exhibits stronger sway and roll responses, which further amplify tension in the M3 mooring relative to the Φ-type VAWT configuration. Due to the smaller equilibrium offsets in vertical and longitudinal drift motion responses, the Φ-type VAWT has shown smaller mooring restoring moment and a comparatively larger pitch response. Overall, the Φ-type VAWT demonstrates stronger dynamic stability.

(5) The PSD analysis of the power coefficient reveals distinct frequency domain characteristics for both configurations. The power coefficient response shows peaks at both the blade passing frequency and the wave excitation frequency, indicating that it is influenced by both aerodynamic and hydrodynamic factors. Due to the stronger unsteady nature of the flow field in the H-type VAWT, its PSD increases significantly in the high-frequency region.

(6) The PSD analysis of the 6-DOF responses for both types of VAWTs shows that the platform's dynamic response is primarily dominated by its natural frequency, wave frequency and its higher-order harmonics. In the low-frequency region, the sway response is mainly driven by low-frequency drift caused by the waves, while the pitch and roll responses exhibit nonlinear coupling between the aerodynamic loading and platform's hydrodynamic restoring forces. Particularly in the roll and yaw responses, the higher-order harmonic components of the waves have a significant impact on the platform's dynamic response. Furthermore, compared to the Φ-type VAWT, the H-type VAWT exhibits more high-frequency peaks in its yaw response, indicating that its complex flow field and aerodynamic instability have a larger effect on the dynamic behavior.

In summary, this study reveals the differences between the Φ-type and H-type VAWTs in terms of aerodynamic performance, wake recovery, and platform motion response through comparative analysis. Its findings provide theoretical insights and guidance for design optimization, engineering applications, and wind farm layout of future floating wind turbines.

7. Limitations and future work

Although the present study provides a full-scale coupled comparison of H-type and Φ-type floating VAWTs, several limitations remain. First, the rotor rotational speed is prescribed in simulations, while inflow-driven rotation and comparative self-starting performance the two rotor configurations are not considered. Second, only a single floating VAWT is investigated, and array effects, wake interaction, and layout optimization are beyond the scope of this work. Third, the simulations are conducted under selected regular wind-wave conditions, while turbulent inflow, irregular waves, current effects, and broader marine environments should be further examined. In addition, the rotor and platform are treated as rigid bodies, and the aeroelastic response and fatigue behavior of blades, support structures, and mooring lines require further investigation.

Future work should focus on several broader directions, including the comparative self-starting performance and operational control of H-type and Φ-type floating VAWTs, array-scale wake interaction, aeroelastic and fatigue assessment, and performance evaluation under more realistic offshore environmental conditions. These studies will help improve the design reliability and engineering applicability of large-scale floating VAWTs.

CRediT authorship contribution statement

Jiarui Dai: Validation, Supervision, Methodology, Investigation, Formal analysis, Data curation. **Haoda Huang:** Writing – review & editing, Validation, Methodology, Investigation. **Qingsong Liu:** Writing – review & editing, Supervision, Resources, Project administration, Funding acquisition, Conceptualization. **Chun Li:** Writing – review & editing, Supervision, Project administration, Funding acquisition.

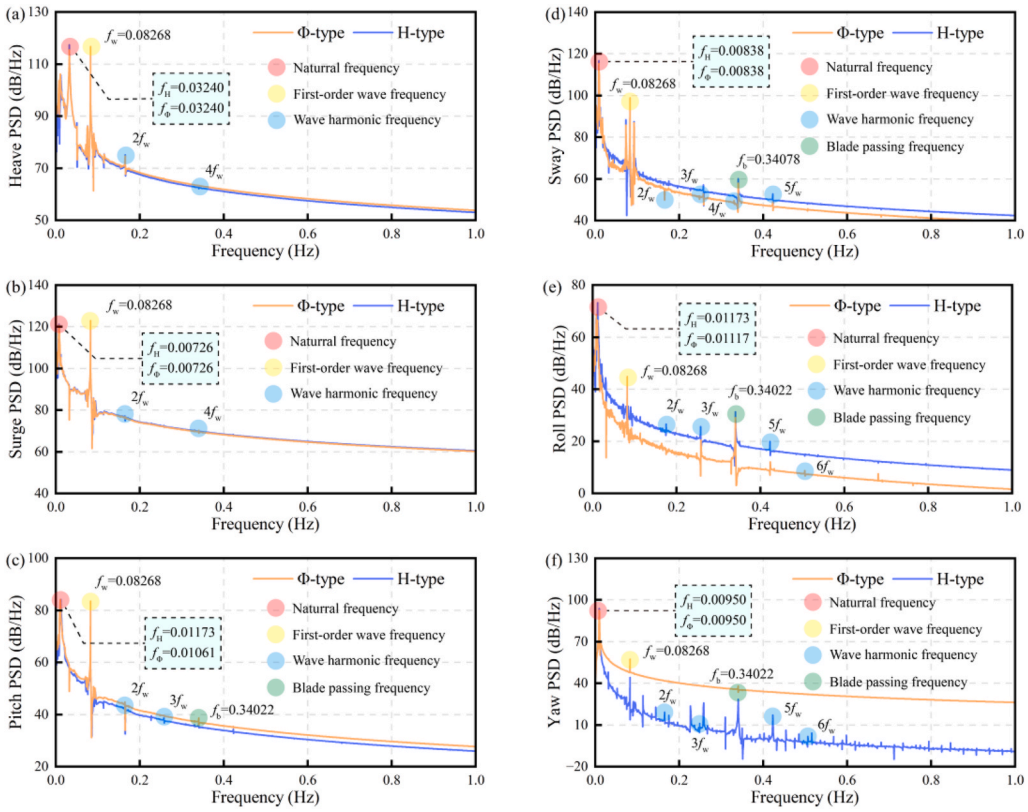


Fig. 27. PSD comparison of 6-DOF response of the two VAWTs.

Gregorio Iglesias: Writing – review & editing, Software. **Musa Bashir:** Writing – review & editing, Formal analysis.

Declaration of competing interest

The authors declare that they have no known competing financial interests or personal relationships that could have appeared to influence the work reported in this paper.

Acknowledgements

This work has received funding from the European Union's Horizon Europe research and innovation program under the Marie Skłodowska-Curie Actions (MSCA) grant agreement No. 101204880 (SMARTBLADE: Integrated System Design and Performance Optimization for Floating Vertical Axis Wind Turbines), as well as support from the National Key R&D Program of China (No. 2024YFA1012500) and the National Natural Science Foundation of China (No. 52376204).

Data availability

No data was used for the research described in the article.

References

[1] IPCC. Climate Change 2023 Synthesis Report. 2023.
[2] IRENA. Renewable energy highlights. 2025.
[3] Sykes V, Collu M, Coraddu A. A review and analysis of optimisation techniques applied to floating offshore wind platforms. Ocean Eng 2023;285:115247.
[4] López-Queija J, Robles E, Jugo J, Alonso-Quesada S. Review of control technologies for floating offshore wind turbines. Renew Sustain Energy Rev 2022;167:112787.
[5] Kumar R, Raahemifar K, Fung AS. A critical review of vertical axis wind turbines for urban applications. Renew Sustain Energy Rev 2018;89:281–91.
[6] Tjiu W, Marnoto T, Mat S, Ruslan MH, Sopian K. Darrieus vertical axis wind turbine for power generation II: challenges in HAWT and the opportunity of multi-megawatt darrieus VAWT development. Renew Energy 2015;75:560–71.
[7] Sutherland HJ, Berg DE, Ashwill TD. A retrospective of VAWT technology. 2011. United States.
[8] Abdolahifar A, Zanj A. A review of available solutions for enhancing aerodynamic performance in Darrieus vertical-axis wind turbines: a comparative discussion. Energy Convers Manag 2025;327:119575.
[9] Ghigo A, Faraggiana E, Giorgi G, Mattiazzo G, Bracco G. Floating vertical Axis Wind Turbines for offshore applications among potentialities and challenges: a review. Renew Sustain Energy Rev 2024;193:114302.
[10] Hand B, Cashman A. A review on the historical development of the lift-type vertical axis wind turbine: from onshore to offshore floating application. Sustain Energy Technol Assessments 2020;38:100646.
[11] Celik Y, Ingham D, Ma L, Pourkashanian M. Design and aerodynamic performance analyses of the self-starting H-type VAWT having J-shaped aerofoils considering various design parameters using CFD. Energy 2022;251:123881.
[12] Ghafoorian F, Mirmotahari SR, Farajyar S, Mehrpooya M, Shafiee M. Performance optimization of Savonius VAWTs using wind accelerator and Guiding Rotor House for enhanced Rooftop urban energy harvesting. Machines 2025;13(9):838.
[13] Ghafoorian F, Mirmotahari SR, Wan H. Numerical study on aerodynamic performance improvement and efficiency enhancement of the savonius vertical axis wind turbine with semi-directional airfoil guide vane. Ocean Eng 2024;307:118186.
[14] Yang H, Zhao M, Tian Z, Yan H, Tian G, Lai W, Zheng X. Aerodynamic response and wake evolution of floating vertical axis wind turbines under different motion modes and parameters. Energy 2025;337:138680.
[15] Sun SY, Liu HJ, Peng HY. Power performance and self-starting features of H-rotor and helical vertical axis wind turbines with different airfoils in turbulence. Energy Convers Manag 2023;292:117405.
[16] Ghasemian M, Ashrafi ZN, Sedaghat A. A review on computational fluid dynamic simulation techniques for Darrieus vertical axis wind turbines. Energy Convers Manag 2017;149:87–100.
[17] Hao W, Abdulshakur A, Zhang L, Li C, Wu F, Mao Q. Performance and mechanism of adaptive pitch control in a floating vertical axis wind turbine with a surge motion. Renew Energy 2024:132896.
[18] Chen Y, Kuang L, Su J, Zhou D, Cao Y, Chen H, Han Z, Zhao Y, Fu S. Investigation of pitch angles on the aerodynamics of twin-VAWT under staggered arrangement. Ocean Eng 2022;254:111385.
[19] Sun X, Zhu J, Hanif A, Li Z, Sun G. Effects of blade shape and its corresponding moment of inertia on self-starting and power extraction performance of the novel bowl-shaped floating straight-bladed vertical axis wind turbine. Sustain Energy Technol Assess 2021;38:100648.
[20] Lei H, Zhou D, Bao Y, Chen C, Ma N, Han Z. Numerical simulations of the unsteady aerodynamics of a floating vertical axis wind turbine in surge motion. Energy 2017;127:1–17.

[21] Lei H, Su J, Bao Y, Chen Y, Han Z, Zhou D. Investigation of wake characteristics for the offshore floating vertical axis wind turbines in pitch and surge motions of platforms. Energy 2019;166:471–89.
[22] Su J, Li Y, Chen Y, Han Z, Zhou D, Zhao Y, Bao Y. Aerodynamic performance assessment of φ-type vertical axis wind turbine under pitch motion. Energy 2021; 225:120202.
[23] Guo Y, Liu L, Li Y, Xiao C, Tang Y. The surge-heave-pitch coupling motions of the Φ-type vertical axis wind turbine supported by the truss Spar floating foundation. J Hydrodyn 2019;31(4):669–81.
[24] Lee H, Poguluri SK, Bae YH. Development and verification of a dynamic analysis model for floating offshore contra-rotating vertical-axis wind turbine. Energy 2022; 240:122492.
[25] Cheng Z, Madsen HA, Chai W, Gao Z, Moan T. A comparison of extreme structural responses and fatigue damage of semi-submersible type floating horizontal and vertical axis wind turbines. Renew Energy 2017;108:207–19.
[26] Luo W, Liu W, Yang M, Chen S, Song X, Wu W. Load characteristics and extreme response of straight-bladed floating VAWT using a fully coupled. J Mar Sci Eng 2023;11(1):185. https://doi.org/10.3390/jmse11010185.
[27] Yang H, Zheng X, Chen Y, Yan H, Chen S, Lai W. Coupled dynamic response and energy conversion characteristics of 10 MW floating vertical axis wind turbine with different configurations. Ocean Eng 2024;309:118610.
[28] Xie L, Huang H, Liu Q, Yue M, Miao W, Li C, Xu Z. Fully coupled aero-hydrodynamic analysis of a floating VAWT with enhanced spar platforms. Energy 2025;341:139362.
[29] Liu Q, Huang H, Iglesias G, Wang J, Bashir M. Fully coupled aero-hydrodynamic analysis of floating vertical axis wind turbines in staggered configurations. Energy 2025;337:138679.
[30] Sergiienko NY, Xue L, Da Silva LSP, Ding B, Cazzolato BS. Statistical analysis of floating hybrid wind–wave energy systems. Appl Energy 2025;401:126669.
[31] Ma Y, Cui L, Zhou H, Bhattacharya S. Hybrid offshore renewable energy harvest system: a review. Energy Convers Manag 2026;348:120654.
[32] Barter GE, Robertson A, Musial W. A systems engineering vision for floating offshore wind cost optimization. Renew Energy Focus 2020;34:1–16.
[33] Zhang W, Calderon-Sanchez J, Duque D, Souto-Iglesias A. Computational Fluid Dynamics (CFD) applications in Floating Offshore Wind Turbine (FOWT) dynamics: a review. Appl Ocean Res 2024;150:104075.
[34] Mind I. SeaTwirl to install 1 MW floating vertical-axis wind turbine in Norway 2022. https://www.inceptivemind.com/seatwirl-install-1-mw-floating-vertical-axis-wind-turbine-norway/27413/.
[35] Liu W, Ding J, Fu J, Zhang Z, Yu J, Hu H, Bashir M, Li S, Yang Y. Comparison of the fully coupled dynamic responses of spar-type integrated wind-current floating energy systems with various tidal turbine layouts. Ocean Eng 2025;325:120866.
[36] Ojo A, Collu M, Coraddu A. Geometric design parameterization and optimization of spar floating offshore wind turbine substructure. Ocean Eng 2025;332:121378.
[37] Somoano M, Trubat P, Guanche R, Molins C. Experimental modelling of a novel concrete-based 15-MW spar wind turbine. Ocean Eng 2024;309:118612.
[38] Ran X, Leroy V, Bachynski-Polić EE. Hydroelastic response of a flexible spar floating wind turbine: numerical modelling and validation. Ocean Eng 2023;286: 115635.
[39] EL Beshbichi O, Xing Y, Ong MC. Comparative dynamic analysis of two-rotor wind turbine on spar-type, semi-submersible, and tension-leg floating platforms. Ocean Eng 2022;266:112926.
[40] Xu X, Day S. Experimental investigation on dynamic responses of a spar-type offshore floating wind turbine and its mooring system behaviour. Ocean Eng 2021; 236:109488.
[41] Yue M, Liu Q, Li C, Ding Q, Cheng S, Zhu H. Effects of heave plate on dynamic response of floating wind turbine Spar platform under the coupling effect of wind and wave. Ocean Eng 2020;201:107103.
[42] Borg M., Collu M. A comparison between the dynamics of horizontal and vertical axis offshore floating wind turbines. Philosophical Transactions of the Royal Society A 2035;2015:373.
[43] Liu Q, Bashir M, Iglesias G, Miao W, Yue M, Xu Z, Yang Y, Li C. Investigation of aero-hydro-elastic-mooring behavior of a H-type floating vertical axis wind turbine using coupled CFD-FEM method. Appl Energy 2024;372:123816.
[44] Tran TT, Kim D-H. Fully coupled aero-hydrodynamic analysis of a semi-submersible FOWT using a dynamic fluid body interaction approach. Renew Energy 2016;92:244–61.
[45] Veritas N. Environmental conditions and environmental loads. Oslo, Norway: Det Norske Veritas; 2000.
[46] Battisti L, Persico G, Dossena V, Paradiso B, Raciti Castelli M, Brighenti A, Benini E. Experimental benchmark data for H-shaped and troposkien VAWT architectures. Renew Energy 2018;125:425–44.
[47] Jonkman J, Musial W. Offshore code comparison collaboration (OC3) for IEA Wind Task 23 offshore wind technology and deployment. Golden, CO (United States): National Renewable Energy Lab.(NREL); 2010.